High-Resolution Data Assimilation for Two Maritime Extreme Weather Events: A comparison between 3DVar and EnKF.

Diego S. Carrió[1], Vincenzo Mazzarella[2], Rossella Ferretti[2]

[1]*Meteorology Group, Department of Physics, University of the Balearic Islands, Palma, Spain*

[2]*CETEMPS, Department of Physical and Chemical Sciences, University of L'Aquila, L'Aquila 67100, Italy*

Eliminado: *a*

Abstract

Populated coastal regions in the Mediterranean are known to be severely affected by extreme weather events. Generally, they are initiated over maritime regions, where a lack of in-situ observations is present, hampering the initial conditions estimations and hence, the forecast accuracy. To face this problem, Data Assimilation (DA) is used to improve the estimation of the initial conditions and their respective forecasts. Although comparisons between different DA methods have been performed at global scales, few studies are performed at high-resolution, focusing on extreme weather events triggered over the sea and enhanced by complex topographic regions. In this study, we investigate the role of assimilating different types of conventional and remote-sensing observations using the variational 3DVar and the ensemble-based EnKF, which are of the most common DA schemes used globally at National Weather Centers. To this aim, two different events are chosen because of both the different areas of occurrence and the triggering mechanisms. Both the 3DVar and the EnKF are used at convection permitting scales to improve the predictability of these two high-impact coastal extreme weather episodes, which were poorly predicted by numerical weather prediction models: (a) the heavy precipitation event IOP13 and (b) the intense Mediterranean Tropical-like cyclone Qendresa. Results show that the EnKF and 3DVar perform similarly for the IOP13 event for most of the verification metrics, although looking at the ROC and AUC scores, the EnKF clearly outperforms the 3DVar. However, the ensemble mean of the EnKF is in general worse than the 3DVar for Qendresa, although some of the ensemble members of the EnKF individually outperforms the 3DVar allowing for gaining information on the physics of the event and hence the benefits of using an ensemble-based DA scheme.

Correspondence: Diego S. Carrió, University of the Balearic Islands, 07122, Cra. Valldemossa km 7.5, Balearic Islands, Palma (Spain)

Email: diego.carrio@uib.es

Keywords: Variational Data Assimilation (3DVar), ensemble data assimilation (EnKF), low-predictable weather events, extreme weather events, high-resolution numerical forecasts.

1. Introduction

The Mediterranean basin is recognized as one of the geographical regions most frequently affected by high impact weather events in the world (Petterssen, 1956). The Mediterranean region has a natural disposition for these events because of its singular orographic features, which include having a relatively warm sea surrounded by complex terrain. This geographical configuration forces the warm and moist airflow to lift, favoring condensation and triggering convection. Hazardous weather events in this region, such as heavy precipitation (e.g., flash floods, snowstorms), cyclogenesis or windstorms (e.g., squall lines, tornadic thunderstorms), produce huge economic, injury and human losses in populated coastal regions (e.g., Romero et al., 1998b; Llasat and Sempere-Torres, 2001; Llasat et al., 2010; Jansa et al., 2014; Flaounas et al., 2016; Pakalidou and Karacosta, 2018; Amengual et al., 2021). Since 1900, more than 500 billion Euros associated with total damages to the property and over 1.3 million fatalities related to hydrometeorological disasters has been registered for the EM-DAT international disaster database[1]. These effects underscore the critical need for accurate and rapid high-resolution weather forecasting systems, aimed at extending the lead time for severe weather warnings, thereby enabling the implementation of effective mitigation strategies to reduce fatalities and economic losses. However, while the accuracy of weather forecasting has significantly improved in recent years, with better representation of physical processes and dynamics, accurate prediction of high impact weather events in terms of their location, timing, and intensity remains a major challenge for the scientific community (Stensrud et al., 2009; Mass et al., 2002; Bryan and Rotunno, 2005; Yano et al., 2018; Torcasio et al., 2021). For this reason, improving the forecast of high-impact weather events becomes an imperative goal.

Deficiencies in the accurate prediction of the location (spatial and temporal), intensity and phenomenology of extreme weather events are tightly related to the accuracy of the initial conditions of the system (Wu et al., 2013). The initial conditions of the hazardous weather events affecting coastal populated regions, are typically poorly estimated, mainly because these weather systems originate over the sea, where there is a lack of *in-situ* observations. Enhanced representations of the initial conditions are typically achieved by blending information from observations into numerical models through sophisticated *Data Assimilation* (DA) techniques (Kalnay, 2003), which accounts not only for the nominal values of the observations and the model, but also accounts for their respective error statistics. DA has been widely used and applied for global numerical weather prediction (NWP) problems (e.g., Eliasen, 1954; Lorenc, 1981; Le Dimet and Talagrand, 1986; Rabier et al., 2000, Whitaker et al., 2008, Carrassi et al., 2018; Albergel, et al., 2020, among others). However, less attention has been paid to convective-scale NWP problems, especially those associated with small scale convective phenomena initiated over regions with sparse observational data coverage, such as the extreme weather events affecting coastal regions in the Mediterranean basin (Carrió et al., 2016; Amengual et al., 2017; Carrió et al., 2019; Lagasio et al., 2019; Amengual et al., 2021; Mazzarella et al., 2021; Torcasio et al., 2021, Capecchi et al., 2021). To improve forecasts of such extreme weather events, accurate high resolution numerical weather models which solve convective scale processes are required, as well as dense observations at high spatial and temporal resolution. These will provide accurate information regarding the convective systems themselves or their environmental conditions. One of the most important sources of convective scale information are ground weather radars that provide three-dimensional data related to the storms at high spatial (order of hundreds of meters) and temporal (order of few minutes) resolution. In addition, weather radars provide thermodynamic and dynamic information of thunderstorms, which are crucial to understand and forecast convective structures. Due to the

[1] https://www.emdat.be/

high spatio-temporal variability of convective structures, a rapid update cycle of the initial state (i.e., analysis) using weather radar observations is required to reduce errors and keep physical balances in the initial conditions. Several studies have shown the positive impact in forecasting severe weather events by assimilating weather radar information (e.g., Xiao and Sun, 2007; Lee et al., 2010; Wheatley et al., 2012; Yussouf et al., 2015; Carrió et al., 2019; Mazzarella et al., 2021).

During the last decades, different DA algorithms have been developed with the aim of improving weather forecasts making use of all available observations in the best possible way. In this context, most of the developed DA methods are based on exploiting Bayes' Theorem (Lorenc, 1986) and making use of different types of approximations. Generally, DA algorithms can be classified into the following three Bayesian-based families: (a) Variational DA (e.g., 3DVar (Barker et al., 2004) or 4DVar (Huang et al., 2009)); (b) Ensemble-based DA, which are based on the *Ensemble Kalman Filter* (EnKF; Evensen, 1994) and (c) Monte-Carlo DA methods. Variational DA minimizes a cost function to obtain the analysis (i.e., the best estimation of the initial conditions). More specifically, variational DA methods provide a (quasi) optimal analysis based on an imperfect forecast (*prior* state or *background*), a set of imperfect observations and their respective error statistics that are prescribed and assumed to be Gaussian, for simplicity. In addition, variational DA algorithms require a linearized and adjoint version of the numerical model, which can be very difficult to develop and maintain. This often involves the use of automatic differentiation tools or complex manual derivation, both of which are error-prone and time-consuming. On the other hand, the ensemble-based DA algorithms do not require the use of linearized or adjoint versions of the model, and they do not use prescribed error statistics. Instead, they compute the error statistics from an ensemble of forecasts, with the main property that these errors are evolving in time as the system evolves. The Monte-Carlo DA method allows the assimilation of observations described with non-Gaussian errors. Particle filters (PF; Van Leeuwen, 2009; Poterjoy, 2016) are a clear example of Monte-Carlo DA algorithm. However, PFs are not well-suited for large multidimensional systems, such as the atmosphere, although a lot of improvements have been achieved recently. In the present study, we will focus on the most widely used DA schemes typically used in major operational weather centers, which are the variational and ensemble-based DA schemes, leaving the Monte-Carlo methods for future work.

Although variational DA schemes have been used in numerical weather prediction for many years (Courtier et al., 1994; Park and Zupanski, 2003; Rawlins et al., 2007), allowing the assimilation of a wide range of different observations, they present a well-known limitation. This limitation is related to the use of a climatological background error covariance matrix to characterize the error statistics, which is kept constant along the assimilation window, where the different observations are distributed at different times. This weakness is specifically linked to the 3DVar method, which typically uses the *National Meteorological Center* (NMC) method (Parrish and Derber, 1992) to generate those static background error covariances using forecast differences over a period of time reasonably close to the event. The error statistics derived from such DA schemes are static, isotropic and nearly homogenous, misrepresenting the true error statistics in space and time, which are inherently flow-dependent, resulting in less accurate analysis. On the other hand, the EnKF DA scheme is designed to provide flow-dependent background error covariances. Some studies have shown the potential of the EnKF spreading information from the observations flow-dependently in comparison with the 3DVar (Yang et al., 2009; Gao et al., 2018). On the other hand, 3DVar techniques require less computational resources and there is no need to build an ensemble compared to EnKF or even simulate the model trajectory as in 4DVar. Therefore, the assimilation with 3DVar takes only a few tens of minutes, making this technique particularly suitable for operational purposes.

To solve convective scale (i.e., grid spacing of a few kilometers) physical processes associated with extreme weather phenomena, high-resolution numerical simulations are required, as well as high resolution initial conditions. This turns in performing computational expensive high-resolution simulations, which poses a significant challenge by limiting the number of ensemble members that can be used in EnKF DA schemes, potentially hindering the estimation of the background error covariance matrix. In this context, which DA method is more suitable? The 3DVar using an *ad hoc* background error covariance matrix or the low-rank background error covariance matrix obtained from the EnKF?

Recent convective-scale DA studies have primarily focused on the mature stage of weather events (e.g., Tong et al., 2005; Fujita et al., 2007; Dowell et al., 2021; Jones et al., 2013; Wheatley et al., 2015; Jones et al., 2016; Gao et al., 2016; Ballard et al., 2016; Gustafsson et al., 2018; Carrió et al., 2019; Mazzarella et al., 2020; Yussouf et al., 2020; Federico et al., 2021; Junjun et al., 2021; Janjić et al., 2022; Wang et al., 2022). However, at this stage, the system is already well-developed and likely impacting the population, limiting the effectiveness of DA in terms of forecast lead time. In such cases, the potential for early warnings and mitigation actions is significantly reduced, as there is little time left to respond and minimize socio-economic impacts. Despite its potential benefits, very few studies have explored the role of DA in the developing stage (e.g., Carrió et al., 2019; Carrió et al., 2022; Corrales et al., 2023), where assimilating observations before convection initiates could significantly improve forecast lead time, providing advanced warnings and allowing decision-makers to act proactively. In this study, we compare the performance of two widely used DA techniques – 3DVar and EnKF – in enhancing the forecast lead time for two extreme weather events initiated over the sea, a data-sparse region where observational constraints pose additional forecasting challenges, affecting populated coastal regions in the Mediterranean basin. It is important to emphasize that this study does not aim to derive statistically significant conclusions. Instead, the main objective is to compare the performance of EnKF and 3DVar in two distinct extreme weather events, each characterized by unique atmospheric conditions and observational limitations. The two extreme weather events selected for this study are: (a) the heavy rainfall episode, IOP13, affecting coastal regions of Italy during October 2012 (Pichelli et al., 2017) and (b) the low-predictable Mediterranean Tropical-like cyclone (medicane), Qendresa, affecting Sicily in November 2014 (Pytharoulis et al., 2017; Pytharoulis, 2018; Cioni et al., 2018; Di Muzio et al., 2019).

On overall, this study aims at:

(a) Assessing the impact of 3DVar in comparison with the EnKF system to predict small-scale extreme weather events initiated over maritime regions with lack of in-situ observations.

(b) Investigate the potential of using 3DVar and EnKF in the developing phase, that is hours before the mature stage of convective systems are reached, to improve forecast lead time and warning capabilities for extreme weather events.

(c) Compare the forecast impact from assimilating in-situ conventional observations in comparison to assimilating high spatial and temporal resolution data from remote sensing instruments.

(d) Provide a quantitative assessment between the different DA schemes by means of using several statistical verification methods.

Eliminado: . P

Eliminado: Recently, a few DA studies at convective scale mainly focused just on the mature stage of the weather event have been carried out

This paper is organized as follows. Section 2 briefly describes the meteorological characteristics of the two events used for comparing the impact of 3DVar and EnKF. In Section 3 the observation dataset that will be assimilated by the different DA methods will be presented. Section 4 briefly explains the main characteristics of the two DA algorithms that will be used in this study. Then, the numerical model configuration and the design of the different experiments for the two different case studies will be described in Section 5 and 6, respectively. Section 7 describes the verification methods used in this study. Results of the different numerical experiments for both meteorological situations are summarized in Section 8. Finally, conclusions are presented in Section 9.

2. Brief Description of Case Studies

Two different extreme weather systems, occurring in the Mediterranean region and affecting populated coastal regions, are considered in this study. The first extreme weather event was associated with heavy rainfall affecting central and northern Italy during October 2012 (IOP13), while the second extreme weather event was associated with the Qendresa medicane affecting southern Sicily, Lampedusa, Pantelleria and Malta islands during November 2014. Both systems were poorly forecasted, and for this reason they are perfect candidates for this intercomparison study.

2.1. The IOP13 Heavy Precipitation Episode

The *IOP13* occurred during the *First Special Observation Period* (SOP1) of the international project *Hydrological cycle in the Mediterranean Experiment* (HyMeX; Drobinski et al., 2014), that was mainly designed to better understand heavy rainfall and flash flooding episodes occurring in the Mediterranean region. The heavy precipitation IOP13 event took place between 14 and 16 October 2012, and it was characterized by a frontal precipitation system associated with a deep upper-level trough extending from northern France towards northern Spain (Fig. 1). It initially affected southern France coastal areas, and afterward it also affected the northern and central parts of Italy. During 15 October, the Italian rain gauge network registered 24-hour accumulated precipitation with peaks reaching 60 mm in central Italy, 160 mm in northeastern Italy and 120 mm in Liguria and Tuscany. During the night of 14 October, a cold front affected the Western Mediterranean region and during 15 October the system rapidly moved from France to Italy, advecting low-level moisture towards the western coast of Italy and Corsica, destabilizing the atmosphere and favoring deep moist convective activity. More details on the synoptic situation and observational data collected during IOP13 can be found in Ferretti et al., 2014.

Eliminado: investigating the mature stage means that t... [1]
Eliminado: impact of
Eliminado: value of improving the atmospheric conditi... [2]
Eliminado: using
Eliminado: to assess the impact of DA in
Eliminado: the
Eliminado: pre-convective
Eliminado: stage
Eliminado: systems to significantly improve the
Eliminado: forecast
Eliminado: lead time, allowing warning systems to act... [3]
Eliminado: compare the performance of two widely us... [4]
Eliminado: also investigate the role of the 3DVar and
Eliminado: the
Eliminado: EnKF
Eliminado: ,
Eliminado: DA methods in improving pre-convective ... [5]
Eliminado: the forecast of two
Eliminado: extreme weather events
Eliminado: initiated over the sea (data sparse region)
Eliminado: and how such improved pre-convective ... [6]
Eliminado: It is important to emphasize that this study ... [7]
Eliminado: Mores specifically,
Eliminado: T
Eliminado: t
Eliminado: he following study aims at: …¶ ... [8]
Eliminado: (a) Assessing the impact of high-resolution ... [9]
Eliminado: the
Eliminado: a high-resolution EnKF system to predict ... [10]
Eliminado: maritime
Eliminado: different areas and with lack of *in-situ* ... [11]
Eliminado: (b) Investigate the potential of using 3DV ... [12]
Eliminado: to improve
Eliminado: thereby improving
Eliminado: forecast lead time
Eliminado: early prediction and warning capabilities ... [13]
Eliminado: (c)
Eliminado: Compare
Eliminado: Quantify the
Eliminado: forecast
Eliminado: impact
Eliminado: from
Eliminado: of assimilating *in-situ* conventional obser ... [14]
Eliminado: (d) Provide a quantitative assessment bet ... [15]
Eliminado: ¶
Eliminado: It is important to emphasize that this stud ... [16]

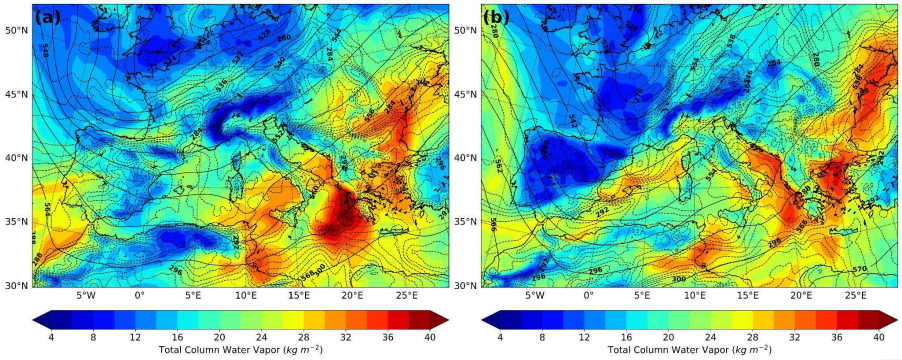

Figure 1. IOP13 ERA5 analyses: 500 hPa geopotential (solid black lines), 925 hPa temperature (dashed grey lines) and total column of water vapor (color shaded areas) at (a) 12 UTC 14 October and (b) 00 UTC 15 October 2012.

2.2. The Qendresa Tropical-Like Cyclone Episode

Among the wide spectrum of maritime extreme weather events, tropical-like Mediterranean cyclones, a.k.a. medicanes (Emmanuel, 2005), draw particular attention to the community mainly because they share similar morphological characteristics with tropical cyclones. Given their tendency to impact densely populated and economically critical areas around the Mediterranean basin, enhancing the accuracy and reliability of medicanes forecasts has become an urgent priority. Here, we focus on the 7 October 2014 medicane (Qendresa; Cioni et al., 2018) that affected the islands of Lampedusa, Pantelleria, Malta and the eastern coast of Sicily. This event was recognized by the community for its limited predictability (Carrió et al., 2017), making it a compelling case study for investigating the performance of the 3DVar and EnKF DA methods. *In-situ* observations located in Malta's airport registered gust wind values exceeding 42.7 m s^{-1} and a sudden and deep pressure drop greater than 20 hPa in 6 hours. Satellite imagery during its mature phase showed a well-defined cloud-free eye surrounded by axisymmetric convective activity, which resembles the morphological properties of classic tropical cyclones.

A deep upper-level trough associated with a cyclonic flow at mid-levels characterized the synoptic situation in the Western Mediterranean from 5 to 8 November 2014. The upper-level trough was associated with an intense PV streamer extending from Northern Europe to Southern Algeria, and the cyclonic flow at mid-levels was dominated by a strong ridge over the Atlantic and a deep trough moving along Western Europe. Late on 7 November, the upper-level trough became negatively tilted, evolving into a deep upper-level cut-off low and the PV streamer disconnected from the northern nucleus (Fig. 2). A small well-defined spiral-to-circular cloud shape formed just south of Sicily and evolved east-northeastward, reaching its maximum intensity over Malta, at midday. Finally, the cyclonic system dissipated as it crossed the Catania (eastern) coast of Sicily. More details on the synoptic situation and observational data collected during this event can be found in Carrió et al., 2017.

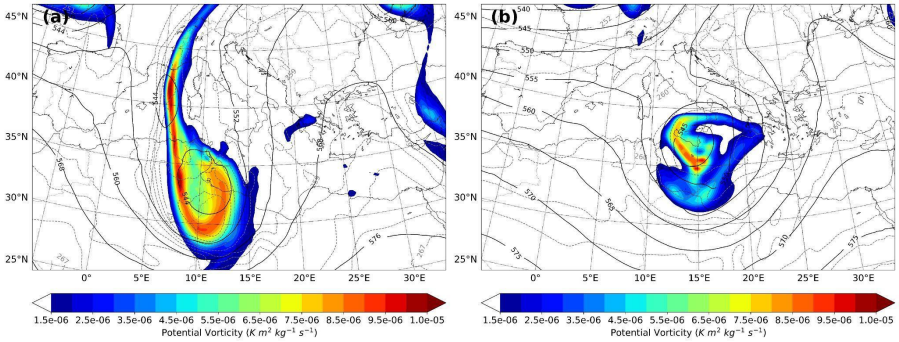

Figure 2. Qendresa ERA5 analyses: 500 hPa geopotential (solid black lines), 500 hPa temperature (dashed grey lines) and 300 hPa Potential Vorticity (color shaded areas) at (a) 00 UTC 7 November and (b) 00 UTC 8 November 2014.

3. Observations Description

In this study, a combination of remote-sensing and *in-situ* observations were assimilated for both case studies. Specifically, the following three types of observations were assimilated: (a) conventional in-situ data from surface meteorological stations, maritime buoys, rawinsondes and aircraft measurements, (b) high temporal and spatial reflectivity data from two Doppler Weather Radars and (c) satellite-derived 3D wind speed and direction data. A summary of the assimilated observations, including their data sources, assimilation frequency, coverage and additional processing is provided in Table 1.

Eliminado: different sources of

Eliminado: available

Eliminado: the two

Eliminado: *in-situ*

Eliminado: derived from satellites

Event	Observation Type	Data Sources	Assimilation Frequency	Coverage	Additional Processing
IOP13	Conventional in-situ data	MADIS (NOAA)	Hourly	Entire Domain	Quality-controlled
IOP13	Radar Reflectivity	Météo-France Doppler Weather Radars (Aleria & Nimes)	Every 15 minutes	Ligurian Sea & Gulf of Genoa	Quality controlled and Interpolated using Cressman Objective Analysis (6 km grid)
Qendresa	Conventional in-situ data	MADIS (NOAA)	Hourly	Mediterranean Region	Quality-controlled
Qendresa	Satellite-Derived	EUMETSAT (SEVIRI	Every 20 minutes	Entire atmosphere	Quality-controlled,

	Winds (RSAMVs)	instrument onboard MSG)		over the Mediterranean Region	superobbing (128x128 km, 25 hPa vertical)

Table 1: Summary of assimilated observations for each case study, including observation type, data sources, assimilation frequency, spatial coverage and additional processing details.

3.1. IOP13 Observations

For the IOP13, we assimilated both *in-situ* conventional data and remote sensing observations from two Doppler Weather Radars. While Italy has a dense national network of radar and in-situ stations, the majority of these datasets were not publicly available. To ensure reproducibility and accessibility, we exclusively used freely available data. For radar observations, we assimilated data from the only two radars providing coverage over the maritime region where the event initiated. Specifically, data from: (a) Aleria radar (9.496ºE, 42.129ºN, 63 m ASL), located on Corsica Island, and (b) Nimes radar (4.502ºE, 43.806ºN, 76 m ASL), located in southern France (Fig. 3a). These two Météo-France polarimetric S-band Doppler Weather Radars, strategically positioned, ensure a good spatial coverage over the Ligurian Sea, the area where triggering and intensification of deep convection occurred, and provide key information about the 3D structure of the convective systems at high spatial and temporal resolution. Aleria and Nimes radars perform 5 and 9 elevation scans every 5 minutes, respectively, and their data are available at the HyMeX's official website (see https://www.hymex.org). Specifically, Aleria radar provides data at 5 elevation angles: 0.57º, 0.96º, 1.36º, 3.16º and 4.57º with a mean frequency of 2.8 GHz. In comparison, Nimes radar provides data at 9 elevation angles: 0.58º, 1.17º, 1.78º, 2.38º, 3.49º, 4.99º, 6.5º, 7.99º and 89.97º, also at the same frequency. It is worth mentioning that Aleria and Nimes radar reflectivity data are provided by the Météo-France operational radar network and undergo rigorous data quality control. This ensures that common radar error sources, such as signal attenuation, ground clutter or beam blocking, are meticulously identified and corrected. Radial velocity from Aleria and Nimes Doppler radars was also available, but because of the low reliability of the data (not quality controlled properly) it was not used in this study. Additionally, conventional in-situ observations were obtained from NOAA's Meteorological Assimilation Data Ingest System (MADIS), a global dataset that provides high-quality, quality-controlled meteorological observations. In particular, we assimilated pressure, temperature, humidity and horizontal wind speed and direction from in-situ instruments such as METARs, maritime buoys, rawinsondes and aircrafts (Fig. 3a).

Overall, the following observations were assimilated for this event:

- Conventional *in-situ* data were hourly assimilated over the entire model domain (Fig. 3a).
- Reflectivity data from Aleria and Nimes weather radars were assimilated every 15 minutes (Fig. 3a).

The high spatial resolution of the reflectivity data poses significant challenges for their direct assimilation, potentially leading to detrimental analysis related with signal aliasing and the violation of the uncorrelated observational error assumptions followed in the derivation of the 3DVar and EnKF analysis equations. To mitigate the adverse effects associated with these issues, the *Cressman Objective Analysis* technique (Cressman, 1959) was used to interpolate

Con formato: Fuente: 11 pto
Con formato: Espacio Antes: 0 pto, Interlineado: Múltiple 1,15 lín.
Con formato: Fuente: 11 pto
Eliminado: ¶
Eliminado: were available
Eliminado: ¶
Eliminado: ¶
Eliminado: Moreover, conventional data were obtained from the NOAA's *Meteorological Assimilation Data Ingest System* (MADIS), which has the main advantage of providing high-level quality-controlled data[2] worldwide. In particular, pressure, temperature, humidity and horizontal wind speed and direction from *in-situ* instruments such as METARs, maritime buoys, rawinsondes and aircrafts (Fig. 3a). In addition to these conventional observations, reflectivity data from two Météo-France polarimetric S-band Doppler Weather Radars, were also available on the Gulf of Genoa. One located in Corsica Island (9.496ºE, 42.129ºN) at 63 m ASL, known as Aleria, and the other located in southern France (4.502ºE, 43.806ºN) at 76 m ASL, known as Nimes (Fig. 3a). These two radars, strategically positioned, ensure a good spatial coverage over the Ligurian Sea, the area where initiation and intensification of deep convection occurred, and provide key information about the 3D structure of the convective systems at high spatial and temporal resolution. The two radars perform 5 and 9 elevation scans every 5 minutes, respectively, and their data are available at the HyMeX's official website (see https://www.hymex.org). Specifically, Aleria radar provides data at 5 elevation angles: 0.57º, 0.96º, 1.36º, 3.16º and 4.57º with a mean frequency of 2.8 GHz. In comparison, Nimes radar provides data at 9 elevation angles: 0.58º, 1.17º, 1.78º, 2.38º, 3.49º, 4.99º, 6.5º, 7.99º and 89.97º, also at the same frequency. It is worth mentioning that Aleria and Nimes radar reflectivity data are provided by the Météo-France operational radar network and undergo rigorous data quality control. This ensures that common radar error sources, such as signal attenuation, ground clutter or beam blocking, are meticulously identified and corrected. Radial velocity from Aleria and Nimes Doppler radars was also available, but because of the low reliability of the data (not quality controlled properly) it was not used in this study.
Eliminado: Hence
Con formato: Espacio Antes: 0 pto
Eliminado: numerical
Eliminado: considered
Con formato: Fuente: (Predeterminada) Arial, 11 pto, Color de fuente: Negro
Con formato: Sangría: Izquierda: 1,27 cm, Espacio Antes: 0 pto, Sin viñetas ni numeración

raw radar observations to a regularly spaced 6 km horizontal grid, as suggested by previous work (i.e., Wheatley et al., 2015; Yussouf et al., 2015). It is important to note that reflectivity observations are typically obtained in polar coordinates, a prerequisite step before applying the Cressman interpolation involves converting them to a Cartesian coordinate system. We have performed several sensitivity tests using different grid space resolution (e.g., 3, 6, 9 km) and we found that using 6 km grid space produces the best analysis. To reduce spurious convective signals and remove excessive humidity the *null-echo* option, which allows assimilation of no precipitation echoes, has been adopted in 3DVAR experiment.

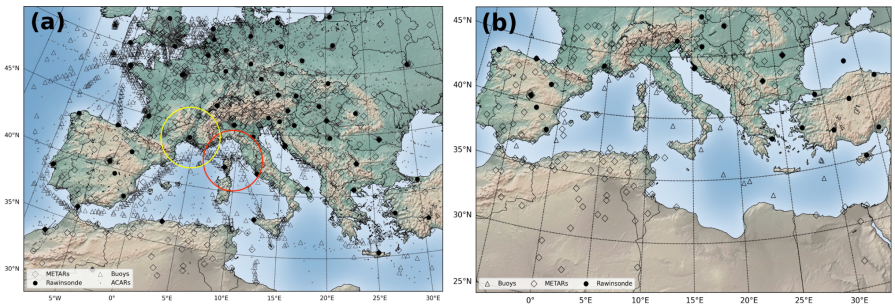

Figure 3. (a) IOP13 Episode: Spatial distribution of *in-situ* observations (gray and black markers) assimilated on the parent numerical domain during 24 h assimilation window from 00 UTC 14 October to 00 UTC 15 October 2012. Doppler Weather Radars located at Nimes and Aleria and their coverage range, depicted in yellow and red circles, respectively. (b) Qendresa Episode: Spatial distribution of *in-situ* observations hourly assimilated during 12 h assimilation window from 12 UTC 6 November to 00 UTC 7 November 2014.

3.2. Qendresa Observations

For the Qendresa event, two different observational sources were publicly available: (a) conventional *in-situ* observations and (b) satellite-derived observations. Conventional *in-situ* observations were obtained from MADIS database. However, only observations from buoys, METAR and rawinsonde were used for this case. It is essential to highlight that observation gaps persist across large areas of the region, particularly over the sea (Fig. 3b), where Qendresa initiated and evolved. As for the IOP13, we were interested in Doppler Weather Radars data to enhance the intensity and trajectory forecasts of Qendresa. Unfortunately, Doppler Weather Radars were not publicly available in the neighborhood of the region where Qendresa initiated and evolved. Instead, we used an alternative high-resolution data source, the so-called *Rapid-Scan Atmospheric Motion Vectors* (RSAMVs; Velden et al., 2017). This dataset provides 3D wind information throughout the entire atmosphere (both speed and direction) at high spatial and temporal resolution (i.e., every 20-min). These observations were particularly valuable for capturing wind field structures over the sea, where conventional observations were sparse or unavailable. This satellite product is obtained using the *Spinning Enhanced Visible and Infrared Imager* (SEVIRI) instrument onboard the *Meteosat Second Generation* (MSG) satellite, which has a scanning frequency as low as 5 minutes. The final product is indeed obtained averaging 4 consecutive images.

Hence, the following observations were assimilated for this event:

Eliminado: episode

Eliminado: but another source of observations

Eliminado: , which

Eliminado: , were available for this event over the sea

- Conventional *in-situ* data from buoys, METAR and rawinsonde for the entire Mediterranean region were hourly assimilated.

- Wind speed and direction from the *Rapid-Scan Atmospheric Motion Vectors* for the entire atmosphere at high spatial and temporal resolution were assimilated every 20 minutes.

Recent studies have shown that upper-level dynamics played a key role in the genesis and the development of Qendresa (Carrió et al., 2017; Carrió, 2022), so the assimilation of RSAMVs is expected to significantly improve its predictability. Here, the infrared channel from RSAMVs (10.8 μm), which contains information throughout the entire atmosphere, was selected to be assimilated (Fig. 4). However, before assimilating RSAMVs, a quality control check to reject non-physical and outlier observations that could deteriorate the quality of the analysis and the successive forecast was applied. In addition, to minimize the effect of having spatial correlated observation errors associated to high density observations, the "*superobbing*" technique consisting in reducing the data density through spatially averaging the observations within a predefined prism is applied (i.e., Pu et al., (2008); Romine et al., (2013); Honda et al., (2018)). Based on the most accurate analysis obtained by multiple sensitivity experiments (not shown) for Qendresa, the RSAMVs data are thinned using a prism with horizontal resolution of 128x128 km^2 and 25 hPa in the vertical.

Eliminado: dimensions

Eliminado: dimension

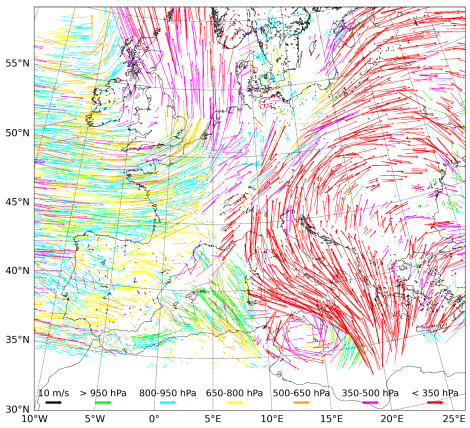

Figure 4. Raw EUMETSAT's RSAMV observations depicted at different vertical levels by infrared channel 10.8 μm at 12 UTC on 7 November 2014 over the Mediterranean region. Wind information is only valid at the center of the wind vectors.

Observations from aircraft (i.e., ACARS) were not assimilated in this case because preliminary assimilation tests indicated a worsening of the results and led to a poorer estimation of the atmospheric state. Buoys, METAR and rawinsonde observations covering the entire Mediterranean region were hourly assimilated.

Finally, observational errors used for the assimilation of the observations associated with both IOP13 and Qendresa are motivated by Table 3 in Romine et al., (2013) with the following minor changes: METAR altimeter (1.5 hPa), marine altimeter (1.20 hPa), METAR and marine

temperature (1.75 K) and RSAMV wind observations (1.4 m s^{-1}). These minor changes are found to provide better data assimilation analysis for the IOP13 and Qendresa extreme weather events in the Mediterranean region. The remaining of the observation errors are the same as the ones in Romine et al., (2013).

4. Data Assimilation Schemes

In the present study, two widely used data assimilation algorithms are used for improving the forecast of extreme weather events initiated and developed over poorly observed maritime regions and affecting densely populated coastal areas. We refer to the *Ensemble Adjustment Kalman Filter* and the variational *3DVar* data assimilation schemes, which are briefly described below.

a) The Ensemble Adjustment Kalman Filter (EnKF)

The *Ensemble Adjustment Kalman Filter* (EAKF; Anderson 2001), which is implemented in the *Data Assimilation Testbed Research* (DART[3]), is used in this study as the former ensemble-based data assimilation technique. The EAKF provides an optimal estimation, in the least square error sense, of the true probability distribution of the state of the atmosphere by merging two main sources of information: (a) the available observations and (b) an ensemble of forecasts (a.k.a. *background*) valid at the analysis time. In particular, the EAKF assimilates the observations serially. This means that the analysis ensemble obtained by the EAKF after the assimilation of the first observation at a given time is then used as the *background* for the next observation at the same analysis time. This is done recursively until all the observations valid at the same analysis time are finally assimilated.

Ensemble covariances used in real-case studies, where only a limited number of ensemble members is feasible, suffers from sampling error, resulting in the generation of spurious correlations that hamper the analysis (Hacker et al., 2007). The detrimental effects of these spurious correlations are mitigated by employing covariance localization functions that go to zero as the distance between the assimilated observation and the grid model point where the analysis occurs, increases (Houtekamer and Mitchell, 1998). In our case, a fifth-order piece-wise rational Gaussian localization function is used (Gaspari and Cohn, 1999). For this study, after several sensitivity simulations it was found that using a half-radius[4] of 230 km in the horizontal and a half-radius of 4 km in the vertical for the horizontal and vertical localizations, respectively, results in the best performance of the DA scheme.

The assimilation of each observation results in a reduction of the ensemble spread, attributed to using a reduced-moderate ensemble size (Anderson and Anderson, 1999). To address this issue and help to maintain the spread, an *adaptive inflation technique* (Anderson and Collins, 2007; Anderson et al., 2009) is applied to the prior ensemble before assimilating the observations. The adaptive inflation technique increases the spread of the ensemble without changing the mean. The inflation value has a probability density distribution described by a mean and a standard deviation. In this study, it was determined that initializing the mean value

Eliminado: high-resolution

Eliminado: simulations, such as the present study,

[3] http://www.image.ucar.edu/DAReS/DART/

[4] The half-radius or cutoff term is defined here as 0.5 times the distance to where the impact of the observation assimilated go to zero. Multiplying the half-radius by 2 results in the maximum distance at which an observation can modify the model state.

of inflation at 1.0 and using a standard deviation of 0.6, yields the best performance of the DA scheme.

b) Three-dimensional Variational Data Assimilation (3DVar)

The 3DVar technique, implemented in WRFDA (Barker et al., 2004), is adopted for the numerical simulations. The 3DVar aims to seek the best estimate of the initial conditions through the iterative minimization of a cost function:

$$J(\mathrm{x}) = \frac{1}{2}\left\{\left(\mathrm{x}-\mathrm{x}_\mathrm{b}\right)^T \mathrm{B}^{-1}\left(\mathrm{x}-\mathrm{x}_\mathrm{b}\right) + \left[\mathrm{y}_\mathrm{o} - \mathrm{H}(\mathrm{x})\right]^T \mathrm{R}^{-1}\left[\mathrm{y}_\mathrm{o} - \mathrm{H}(\mathrm{x})\right]\right\}$$

Eliminado: $J(\mathbf{x}) = \frac{1}{2}\left\{\left(\mathbf{x}-\mathbf{x}_b\right)^T \mathbf{B}^{-1}\left(\mathbf{x}-\mathbf{x}_b\right)+\left[\right.\right.$

where **B** and **R** are the background and observation error matrices, respectively; **x** is the state vector; $\mathbf{y}_o$ is the observations, $\mathbf{x}_b$ is the first guess and *H* is the forward (non-linear) operator that converts data from model space to observation space.

The solution of the above cost function J consists in finding a state $\mathbf{x}_a$ (analysis), that minimizes the distance between the observations and the background field. However, in a model with 10^6 degrees of freedom, the direct solution is computationally expensive. To reduce the complexity and calculate $\mathbf{B}^{-1}$ more efficiently, a pre-conditioning is applied by transforming the control variables, respectively, pseudo relative humidity, temperature, u, v, and surface pressure, as $\mathbf{x} - \mathbf{x}_b = \mathbf{U}v$, where v is the control variable and **U** the transformation operator.

The background error covariance matrix **B** matrix plays a key role in the assimilation process by weighing and smoothing the information from observations and by ensuring a proper balance between the analysis fields. The *National Meteorological Center* method (NMC; Parrish and Derber, 1992) was used to model the B matrix. This method evaluates the differences between two short-term forecasts valid at the same time but with different lead time, 12h and 24h, respectively, to generate the forecast error covariance matrix **B**. Consistent with several papers (Hung et al. 2023; Fitzpatrick et al., 2007; Mazzarella et al., 2020, 2021) showing positive results, a two-week period was used for the calculation of the B matrix in this study. Recently, several works (Wang et al., 2013; Li et al., 2016; Shen et al., 2022; Ferrer Hernandez et al., 2022) show the benefit of using a slightly different approach for the **B** matrix (CV7) in assimilating radar reflectivity, besides in precipitation forecast accuracy. The CV7 differs from the others by using empirical orthogonal functions (EOFs) to represent the vertical covariance instead of a vertical recursive filter. Moreover, the control variables are in eigenvector space, and they are the following: u, v, temperature, pseudo relative humidity (RH_s), and surface pressure (P_s). Therefore, CV7 option has been used to generate the **B** matrix for both case studies. In this study, the weak penalty constraint (WPEC) option (Li et al., 2015) implemented in WRFDA has been activated to improve the balance between the wind and thermodynamic state variables, enforcing the quasi-gradient balance on the analysis field.

5. Model set-up

The mesoscale Advanced Research Weather Research and Forecasting Model (WRF; Skamarock et al., 2008) version 3.7 is used in this study. WRF solves a fully compressible and non-hydrostatic set of equations, using a η terrain-following hydrostatic-pressure vertical

coordinate. The Arakawa C-grid staggering scheme and a third-order Runge-Kutta time-integration, to improve the precision of the numerical solutions, are used. Because IOP13 and Qendresa episodes took place in different locations and with different conditions, two different model configurations were used. For the IOP13 episode, a one-way nested model configuration with the parent domain centered over the Western Mediterranean Sea, covering Central Europe and North Africa, with a horizontal grid-resolution of 15 km (168x247) and a nested domain centered over Gulf of Genoa with a horizontal grid-resolution of 3 km (250x250) were used (Fig. 5a). A total of 51 vertical model levels were employed, spanning from the surface to 50 hPa, with a denser distribution of levels in the lower atmosphere than in the upper for both domains. For Qendresa, a one-way nested model configuration is also used, but now the parent domain is centered over the Central Mediterranean Sea, covering most of the European region and the northern part of Africa (Fig. 5b), using a horizontal grid resolution of 15 km (245x245). The nested domain is centered over Sicily (Southern Italy) using a grid resolution of 3 km (253x253). Both numerical domains use a 51 terrain-following η levels up to 50 hPa, as in the IOP13 case.

For the EnKF DA experiments, initial and boundary conditions used to perform the simulations associated with IOP13 were obtained from the *European Center of Medium Range Weather Forecasts Global Ensemble Prediction System* (EPS-ECMWF), which stored meteorological fields using a horizontal and vertical spectral triangular truncation of T639L62 (i.e., ~32 km grid resolution in the horizontal). In particular, the EPS-ECMWF provides 51 different initial and boundary conditions from 50 perturbed ensemble members plus a control simulation. However, due to unfeasible computational resources required to run our numerical simulations at high resolution, here we will use an ensemble consisting of 36 members. This configuration is analogous to the one used at the internationally prestigious *National Oceanic and Atmospheric Administration - National Severe Storms Laboratory* (NOAA-NSSL) in Norman (Oklahoma, USA) to improve predictability of tornadoes. To obtain the desired 36-member ensemble, a *Principal Components Analysis* and *K-mean* clustering technique were used together to select the 36 ensemble members from the EPS-ECMWF showing more dispersion over the entire numerical domain (see Garcies and Homar, 2009 and Carrió et al., 2016 for more details using these techniques). To perform Qendresa DA simulations, the initial and boundary conditions were obtained following the same methodology explained above for the IOP13 case, i.e., using an ensemble of 36 members obtained from the EPS-ECMWF. On the other hand, the initial and boundary conditions for 3DVar simulations are provided by the *Integrated Forecast System* (IFS) global model from the ECMWF, with a spatial resolution of 0.1° x 0.1° and updated every 3 hours.

Eliminado: Both domains were characterized to have

Eliminado: 51 vertical model levels, from surface to 50 hPa, with higher density of levels in the lower part of the atmosphere than in the upper

Eliminado: for both domains were used

Eliminado: two

Eliminado: grid

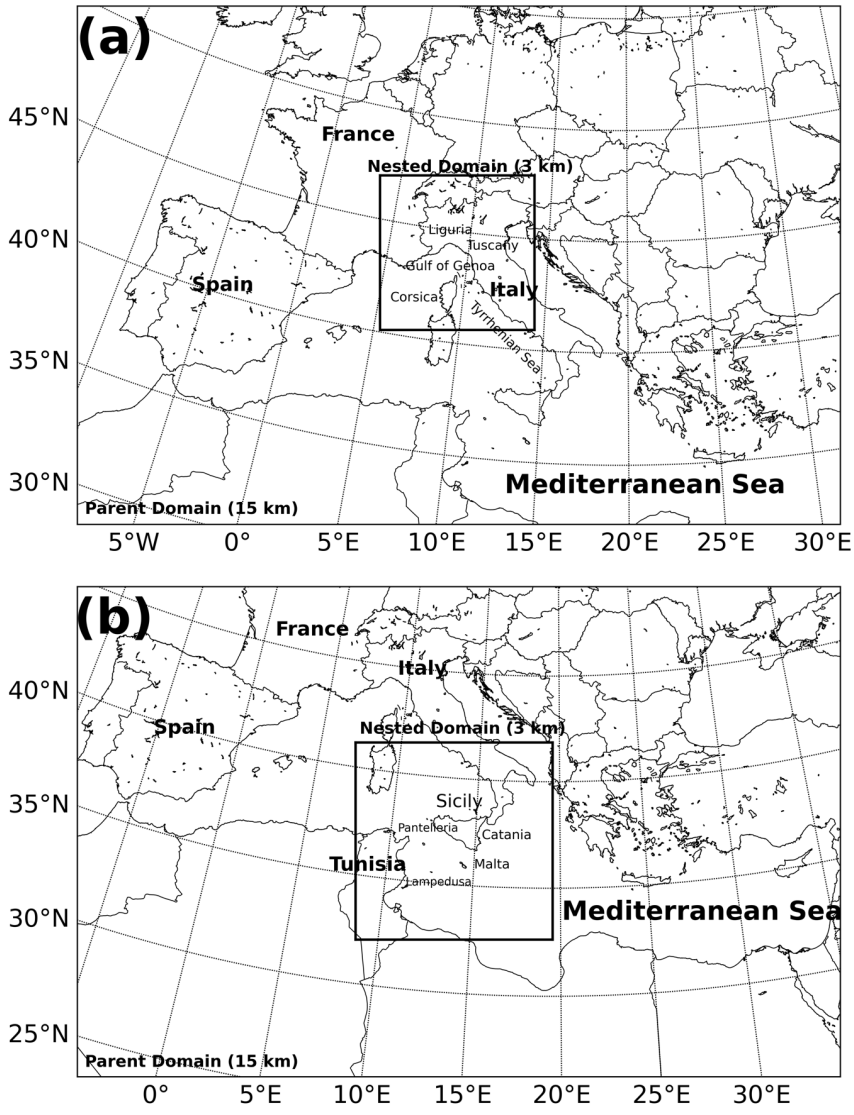

Figure 5. Mesoscale and storm-scale numerical domains used in this study for the (a) IOP13 and (b) Qendresa episodes, respectively.

To estimate the uncertainties of WRF, which is a necessary information for the EnKF, a multiphysics ensemble is built for both the IOP13 and Qendresa event (e.g., Stensrud et al., (2000); Wheatley et al., (2012)), where each ensemble member gets a different set of parameterizations (see Table 2). In particular, the diversity in our ensemble consists of (a) two

short- and long-wave radiation schemes [Dudhia (Dudhia, 1989) and RRTMG (Iacono et al., 2008)], (b) three cumulus parameterizations schemes [Kain-Fritsch (KF; Kain and Fritsch, 1993; Kain, 2004), Tiedtke (Tiedtke, 1989) and Grell-Freitas (GF; Grell and Freitas, 2013)] and (c) three planetary boundary layer schemes [Yonsei University (YSU; Hong et al., 2006), Mellor-Yamada-Janjic (MYJ; Janjic, 1990, 2001), and Mellor-Yamada-Nakanishi-Niino level 2.5 (MYNN2; Nakanishi and Niño, 2006, 2009)]. Two widely used physics parameterizations are adopted for the microphysical processes and land surface interactions, the New Thompson (Thompson et al., 2008) and Noah (Tewari et al., 2004) schemes, respectively. Note that the above-mentioned physical parameterizations are used for both the large-scale ensemble in the parent domain and the storm-scale ensemble in the nested domain, except for the cumulus parameterization that is only applied in the parent domain ensemble. On the other hand, for the WRF deterministic simulation using 3DVar, the microphysical processes are parametrized by using the New Thompson scheme, while a YSU scheme is adopted for PBL. Long- and short-wave radiation are considered through a RRTMG and Dudhia scheme, respectively; while Kain-Fritsch scheme is used for the convection, except for the inner domain where it is explicitly resolved.

Table 2: Multiphysics parameterizations used to generate the 36-member ensemble for the EnKF experiments in IOP13 and Qendresa episodes. PBL, SW and LW stand for planetary boundary layer, short-wave and long-wave, respectively.

Multiphysic Configuration											
Ens. Memb.	**MP**	**CU**	**PBL**	**Land Sfc**	**SW/LW Rad.**	**Ens. Memb.**	**MP**	**CU**	**PBL**	**Land Sfc**	**SW/LW Rad.**
1	New Thompson	KF	YSU	Noah	Dudhia	**19**	New Thompson	KF	YSU	Noah	Dudhia
2	New Thompson	KF	YSU	Noah	RRTMG	**20**	New Thompson	KF	YSU	Noah	RRTMG
3	New Thompson	KF	MYJ	Noah	Dudhia	**21**	New Thompson	KF	MYJ	Noah	Dudhia
4	New Thompson	KF	MYJ	Noah	RRTMG	**22**	New Thompson	KF	MYJ	Noah	RRTMG
5	New Thompson	KF	MYNN2	Noah	Dudhia	**23**	New Thompson	KF	MYNN2	Noah	Dudhia
6	New Thompson	KF	MYNN2	Noah	RRTMG	**24**	New Thompson	KF	MYNN2	Noah	RRTMG
7	New Thompson	GF	YSU	Noah	Dudhia	**25**	New Thompson	GF	YSU	Noah	Dudhia
8	New Thompson	GF	YSU	Noah	RRTMG	**26**	New Thompson	GF	YSU	Noah	RRTMG
9	New Thompson	GF	MYJ	Noah	Dudhia	**27**	New Thompson	GF	MYJ	Noah	Dudhia
10	New Thompson	GF	MYJ	Noah	RRTMG	**28**	New Thompson	GF	MYJ	Noah	RRTMG
11	New Thompson	GF	MYNN2	Noah	Dudhia	**29**	New Thompson	GF	MYNN2	Noah	Dudhia
12	New	GF	MYNN2	Noah	RRTMG	**30**	New	GF	MYNN2	Noah	RRTMG

	Thompson						Thompson					
13	New Thompson	Tiedke	YSU	Noah	Dudhia	**31**	New Thompson	Tiedke	YSU	Noah	Dudhia
14	New Thompson	Tiedke	YSU	Noah	RRTMG	**32**	New Thompson	Tiedke	YSU	Noah	RRTMG
15	New Thompson	Tiedke	MYJ	Noah	Dudhia	**33**	New Thompson	Tiedke	MYJ	Noah	Dudhia
16	New Thompson	Tiedke	MYJ	Noah	RRTMG	**34**	New Thompson	Tiedke	MYJ	Noah	RRTMG
17	New Thompson	Tiedke	MYNN2	Noah	Dudhia	**35**	New Thompson	Tiedke	MYNN2	Noah	Dudhia
18	New Thompson	Tiedke	MYNN2	Noah	RRTMG	**36**	New Thompson	Tiedke	MYNN2	Noah	RRTMG

6. Design of IOP13 and Qendresa Experiments

To quantitatively assess the benefits of assimilating different types of observations using the 3DVar and the EnKF DA schemes, a few numerical experiments are performed. A reference experiment without any data assimilation (NODA) is carried out. Then, several numerical experiments using different types of observations for the assimilation are performed. Only conventional *in-situ* observations are assimilated using the 3DVar and the EnKF, for the first set of experiments (SYN). All available observations (i.e., conventional, radar based and satellite derived data) are assimilated using both 3DVar and EnKF, for the second type of experiments (CNTRL). The comparison between these numerical experiments will provide information on which DA scheme and observation is performing better for these weather events. The DA experiments mainly consist of two phases: the first one is related to the data assimilation procedure, where different types of observations are assimilated by the variational 3DVar and the ensemble-based EnKF DA schemes; the second phase is associated with the free model run initialized using the initial conditions obtained during the first phase. The total forecast time is 24 h and 36 h for IOP13 and Qendresa, respectively. For IOP13, a further simulation lasting 6-hour from 18 UTC 13 October to 00 UTC 14 October 2012 (Carrió et al., 2019) is performed (Fig. 6) to reduce spin-up problems related to the direct downscaling from global ECMWF analysis (32 km grid resolution) to the WRF parent domain used in our simulations (16 km grid resolution). This procedure improved the DA for IOP13, but it had a small impact for Qendresa.

Therefore, the following model simulations were performed:

- No Data Assimilation (NODA)
- Only conventional *in-situ* observations are assimilated using the 3DVar and the EnKF (SYN)
- All available observations (i.e., conventional, radar based and satellite derived data) are assimilated using both 3DVar and EnKF (CNTRL)

The comparison between the DA experiments and NODA allows us to assess the impact of the DA procedure. On the other hand, the comparison between SYN and CNTRL will allow for assessing the role of radar and/or satellite data, especially for the events originated in the area

Eliminado: T

where observations are not available. Moreover, the assimilation of the radar and/or satellite will produce important information on the triggering phase of both events developing on the sea.

6.1. CNTRL Experiments

For IOP13, the CNTRL experiment is designed to assimilate both *in-situ* conventional and reflectivity observations from Aleria and Nimes Doppler weather radars. The assimilation of the reflectivity is expected to improve the forecast of this event by significantly improving the initial conditions over the sea, where convective activity initiated and evolved into deep convection affecting coastal populated areas of Italy. As briefly described in the previous section, this experiment consists of three stages: 1) the spin-up of the storm-scale domain is accounted for by running the WRF model during 6 hours from 18 UTC 13 October to 00 UTC 14 October 2012. Note that for the 3DVar experiment, the spin-up is accounted for by just initializing WRF with the deterministic analysis from the IFS ECMWF. However, for the EnKF counterpart, the spin-up is accounted by initializing the 36-member ensemble at 18 UTC 13 October; 2) *in-situ* conventional observations were hourly assimilated during 24 hours from 00 UTC 14 October to 00 UTC 15 October, meanwhile reflectivity observations were assimilated using a Rapid-Update Assimilation Cycle every 15 minutes during a period of 6 hours, from 18 UTC 14 October to 00 UTC 15 October (Fig. 6); 3) a 24-h ensemble (deterministic) forecast until 00 UTC 16 October, using the recently obtained initial conditions, is performed by the EnKF (3DVar).

For the Qendresa episode, CNTRL experiment is designed to assimilate both *in-situ* conventional and RSAMV observations. The assimilation of RSAMV observations is expected to improve the representation of the atmospheric circulation at upper-levels, whereas the assimilation of surface conventional observations is expected to enhance the one at low-levels. The Qendresa CNTRL experiment consists of two main phases: 1) *in-situ* conventional and satellite derived RSAMV observations are hourly and 20-min assimilated, respectively, during a 12-h period from 12 UTC 6 November to 00 UTC 7 November 2014 to end up with the last analysis at the end of the assimilation window (i.e., 00 UTC 7 November); 2) a free 36-h ensemble (deterministic) forecast is performed by the EnKF (3DVar) from 00 UTC 7 November to 12 UTC 8 November 2014 (Fig. 6).

6.2. SYN Experiments

For IOP13, the SYN experiment assesses the impact of *in-situ* conventional observations, which are crucial to characterize mesoscale atmospheric circulation. Analogous to the CNTRL, SYN follows the same three phases, but in the second phase only the hourly *in-situ* conventional observations from 00 UTC 14 October to 00 UTC 15 October 2012 are assimilated. The analysis obtained from the assimilation stage is used as initial conditions for running the free forecast for 24h, in the third phase (Fig. 6).

Similarly, also for Qendresa, in the SYN experiment only *in-situ* conventional observations are hourly assimilated for 12 hours, from 12 UTC 6 November to 00 UTC 7 November 2014 (Fig. 6).

Eliminado: 21

Eliminado: b

Eliminado: and

Eliminado: e

Eliminado: a

Eliminado: d

6.3. NODA Experiments

For the IOP13, NODA experiment is a direct downscaling from EPS-ECMWF boundary and initial conditions valid at 18 UTC 13 October to 00 UTC 16 October 2012 (Fig. 6). The comparison among NODA, CNTRL and SYN will provide us with valuable information on the impact of assimilating different sources of observations.

For Qendresa, NODA experiment is simply a direct downscaling of 36 hours from EPS-ECMWF at 00 UTC 7 November to 12 UTC 8 November 2014 (Fig. 6). Here again, it is important to note that the choice of starting NODA at 00 UTC 7 November instead of starting at 12 UTC 6 November was made intentionally to extract general conclusions applicable possibly to an operational framework.

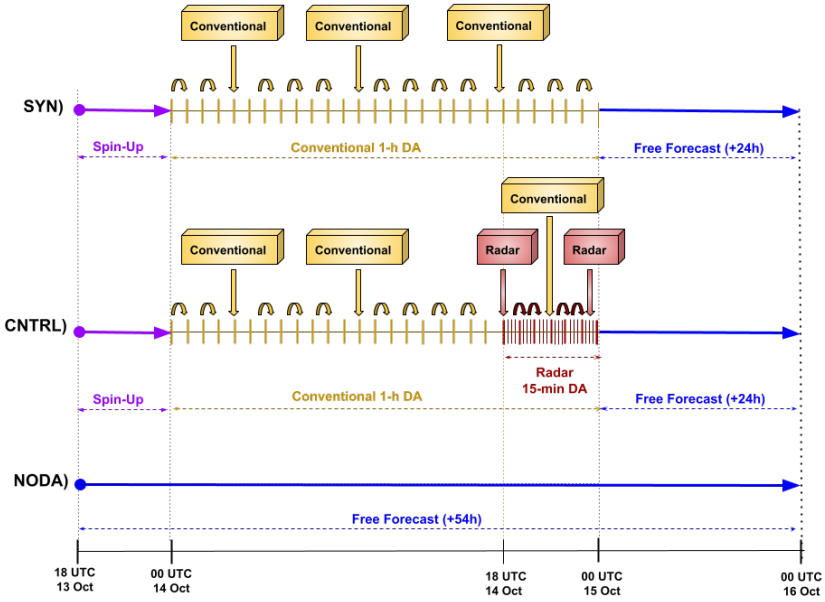

Eliminado: 00

Eliminado: 5

Eliminado: To the aim of simulating an operational framework, the NODA experiment starts at 00 UTC 15 October, instead of starting at 18 UTC 14 October (Fig. 6c). With this choice of the starting time, one could answer the question of which forecast system we should use to predict a 24-48 h forecast. Should we simply perform a simple downscaling using the last analysis obtained from a global model, or should we start our simulation with a previous analysis but now using DA at high temporal and spatial resolution to enhance the estimation of the initial conditions?

Eliminado: f

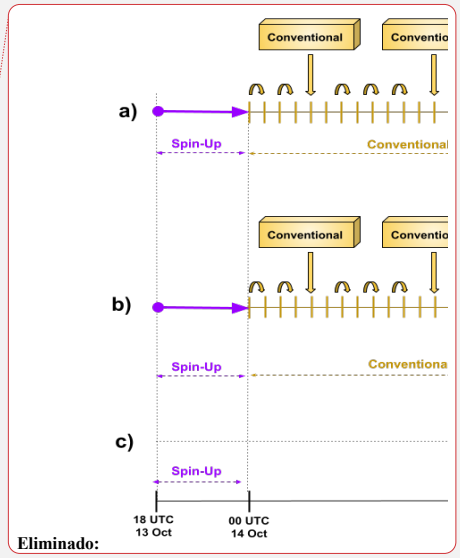

Eliminado:

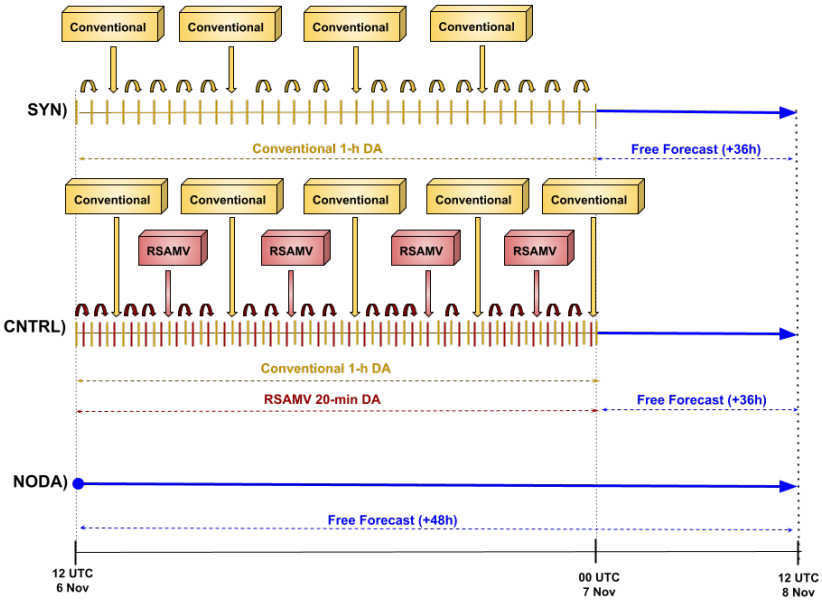

Figure 6. Schematic representation of the main numerical experiments performed in this study for the IOP13 (top panel) and Qendresa (bottom panel) episodes, respectively. SYN, CNTRL and NODA experiments are illustrated for each case, highlighting their respective configurations and assimilation strategies.

7. Verification Methods

To quantitatively evaluate the performance of the EnKF and the 3DVar and their impact on the short-term forecast of these two extreme weather events, various verification scores are used. Given the different nature of the weather phenomena associated with these episodes, the selection of verification scores is tailored specifically to each event. For the IOP13 heavy precipitation event (Fig. 7a), the model verification was performed using the observed accumulated precipitation field over different time windows (e.g., 3 hours, 6 hours or 9 hours). More specifically, the accumulated precipitation was computed using observations from the *Italian Department of Civil Protection*. However, the spatial distribution of rain gauges is not homogenous and there are regions where a lack of rain gauges is present. To address these issues, three sub-regions are chosen where the heavy precipitation event was well recorded by the weather stations (see R1, R2 and R3 in Fig. 7b). Conversely, for the Qendresa tropical-like cyclone, a limited number of *in-situ* observations were present since it initiated and moved over the sea during its lifecycle, and radar-data were not available. Consequently, IR satellite imagery was the primary source of data to approximately estimate Qendresa's trajectory (Fig. 7c). Regarding the intensity of Qendresa, since the cyclone's center passed over Malta island,

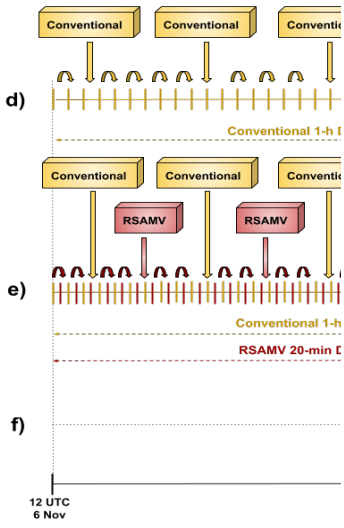

Eliminado:

Eliminado: for the IOP13

Eliminado: and Qendresa are shown in the upper and lower panels, respectively.

Eliminado: are shown in (a), (b

Eliminado:) and (c) panels, respectively, meanwhile the ones corresponding to Qendresa are shown in (d), (e) and (f), respectively.

Eliminado: ¶

reaching its minimum mean sea level pressure (MSLP) of 985 hPa, METAR data from Malta's airport was also used to verify the cyclone's intensity (Fig. 7d).

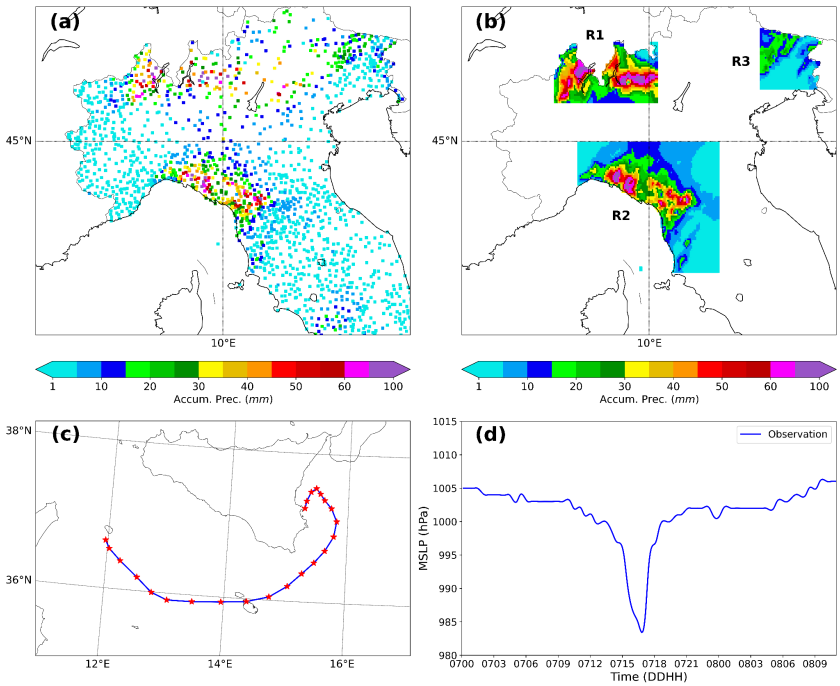

Figure 7. (a) Example of the 12-h accumulated precipitation estimated values and their spatial distribution from the *Italian Department of Civil Protection* rain gauges. (b) Linear interpolation of 12-h accumulated precipitation values into the three target areas where verification has been performed. (c) Observed track of Qendresa medicane viewed from infrared satellite imagery. (d) Surface pressure (hPa) data obtained from the METAR station at Malta's airport.

To quantitatively assess the short-term (i.e., first 6-9 hours) precipitation forecast for the IOP13 initialized using the analysis from the 3DVar and EnKF DA techniques, the *Filtering Method*, the *Relative Operating Characteristics* (ROC; Mason, 1982; Stanski et al., 1989; Swets, 1973) and the *Taylor Diagrams* (Taylor, 2001) were used. We avoid using the conventional point-by-point approach, which has been shown to have serious limitations in the evaluation of high-grid spatial and temporal precipitation field resolutions (Roberts, 2003). More specifically, as *Filtering Method* we use the *Fraction Skill Score* (FSS; Roberts and Lean, 2008), which is commonly used to quantitatively assess precipitation. A preliminary interpolation of the forecast and the observations onto a common regular mesh of 3 km is performed to compute FSS. Then the comparison is carried out within a region of 3x3 grid cells around each grid cell. The FSS can be used to determine the scale over which a forecast system has sufficient skill (Mittermaier, 2010). The FSS ranges from 0 to 1, being 1 a perfect match between model and observations. In addition to the ROC curves, the *Area Under the ROC Curve* (AUC; Stanski

et al., 1989; Schwartz et al., 2010), which is also widely used to quantitatively assess the quality of weather forecasts, will be also used in this study. For a perfect forecast, AUC is equal to 1.

For Qendresa, the *Whisker diagrams* (Tukey, 1977) and the *Probability Distribution of the Cyclone Center Occurrence* **(PCCO)**, which was based on the *Kernel Density Estimation* (KDE; Bowman and Azzalini, 1997; Scott, 2015; Silverman, 2018), were used to validate the simulations. More specifically, the KDE is used to compute the probability of having the center of the cyclone over the entire numerical domain. The main idea behind KDE is to place a "kernel" (i.e., a probability distribution function) at each data point, and then sum up the kernels to estimate the overall probability density function. The kernel is typically chosen to be a smooth function, such as a Gaussian, that decays to zero as the distance from the data point increases. The width of the kernel is controlled by a parameter called the bandwidth, which it turns out to be one of the limitations of the KDE technique. In this case, we found that the optimal bandwidth is 20 km, which is within the meso β scale, i.e. a typical length scale for convective cells. Here, a 2-dimensional KDE will be applied over each cyclone center (*lat*, *lon* coordinates) identified for the different simulations (i.e., EnKF vs 3DVar). In this way, we will infer the most probable track of Qendresa for the different simulations, thereby identifying which is the best DA technique and which provides better estimations of Qendresa medicane's track.

8. Results

As discussed in the previous section, the abovementioned verification techniques were applied for the two extreme events. The results are described in the following subsections.

Eliminado: To quantitatively estimate the impact on the short-range forecast from assimilating the different types of observations considered in this study, using the 3DVar and the EnKF, …

Eliminado: Because of the differences in their features, we used the *Filtering method*, the *Relative Operating Characteristics* (ROC) and *Area Under the ROC curve* and the *Taylor diagrams* for IOP13, and the *Whisker diagrams* and the *Probability Distribution of Cyclone Center Occurrence* for Qendresa.

Eliminado: here

8.1. Statistical analysis: IOP13 Episode

Because IOP13 was a heavy rainfall episode, to quantitatively assess the impact on the short-range forecasts from assimilating both *in-situ* conventional and reflectivity observations from Doppler weather radars using the 3DVar and the EnKF DA algorithms, the accumulated precipitation field will be used.

8.1.1. Filtering Method

The FSS associated with the 3-h accumulated precipitation field is computed independently for the three sub-regions R1, R2 and R3, which are highlighted in Fig. 7b. These regions were chosen due to their higher observation density, allowing for a more reliable evaluation. The analysis is carried out using two precipitation thresholds: 5 mm·h-1 (moderate rainfall) and 10 mm·h-1 (heavy rainfall). In general, except for R3, the comparison in terms of FSS (Fig. 8 a-f) shows that at the initial forecast time and during the first 6 hours, DA simulations (EnKF and 3DVar) outperform the NODA simulation (without assimilation). Among the DA simulation, EnKF generally outperforms 3DVar in R1 and R2, especially for the higher precipitation threshold (10 mm·h-1). As expected, CNTRL experiments for both 3DVar and EnKF provide higher FSS values compared to SYN experiments, where reflectivity observations were not considered.

In R3, the results show an unexpected behavior when using the moderate threshold (5 mm·h-1) (Fig. 8c), where NODA outperforms DA simulations during the first few hours. This anomaly could be explained by two factors: (1) the moderate precipitation threshold, which may not capture significant precipitation differences, and (2) the fact that in the first few hours, precipitation in R3 is minimal since the deep convection system has not yet reached this region. This interpretation is reinforced when examining the higher precipitation threshold (10 mm·h-1) (Fig. 8f), where all methods exhibit similarly poor skill in the early forecast hours, indicating that precipitation is still too weak to be meaningfully assessed. However, after 6-9 hours, as expected, DA simulations outperform NODA in all sub-regions.

To be noticed, the CNTRL simulations do not consistently show better FSS scores than SYN simulations during the first hours, for R1. This could be due to the short-lived impact of radar reflectivity assimilation, which in past studies has been shown to last no longer than 2-4 hours for 3DVar and EnKF, respectively. These findings align with previous studies, which reported similar behavior regarding the transient impact of reflectivity DA (Carrió et al., 2016; Carrió et al., 2019).

Finally, we also computed the Root Mean Squared Error (RMSE) for the precipitation field over the first 24 hours of free forecast for both DA and NODA experiments (Fig. 8g-i). For 3DVar and NODA, RMSE is calculated from the deterministic forecast, while for EnKF, it is computed from the ensemble mean precipitation field. Overall, DA experiments exhibit lower (better) RMSE scores compared to NODA, confirming the positive impact of data assimilation on forecast accuracy. Among the DA experiments, EnKF consistently outperforms 3DVar in all regions, suggesting a better representation of precipitation variability and improved initial conditions.

Eliminado: The FSS associated with the accumulated precipitation field is computed independently for the three sub-regions R1, R2 and R3 highlighted in Fig. 7b, where the density of observation was higher, using as threshold

Eliminado: 5

Eliminado: 1 mm·h^{-1}

Eliminado: (moderate rainfall) and 10 mm·h-1 (heavy rainfall)

Eliminado: . In general, the comparison in terms of FSS (Fig. 8 a-

Eliminado: f

Eliminado: c) shows that EnKF outperforms 3DVar during the first 7 hours of free forecast in the three sub-regions. As it was expected, the CNTRL experiments for both the EnKF and 3DVar outperform the SYN experiments, where reflectivity observations were not considered. Moreover, Fig. 8a shows that the 3DVar-CNTRL provides the worst scores, except for the first few hours of simulation where 3DVar-CNTRL performs better than 3DVar-SYN. This is because the information ingested from the radar using the 3DVar in that region is lasting no longer than 2 hours. Something similar happens with the EnKF after 4 hours. These results would agree with past studies, showing similar behaviors (Carrió et al., 2016; Carrió et al., 2019).

Eliminado: ¶

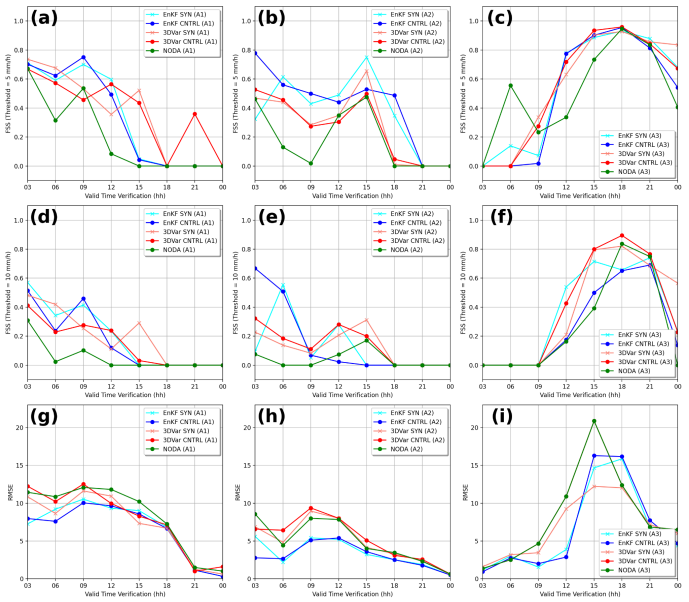

Figure 8. Upper panels: Evolution of the FSS during the first 24-h hours of free forecasts for 3-h accumulated precipitation in the Italian sub-regions: R1 (first column), R2 (second column) and R3 (third column). Two thresholds are used: > 5 mm·h^{-1} (first row) and > 10 mm·h-1 (second row). Lower ponels: Evolution of the RMSE associated with each experiment during the first 24 hours of free forecast in the different sub-regions. Simulations assimilating both conventional and radar observations (CNTRL) and simulations assimilating only conventional observations (SYN) associated with the 3DVar and the EnKF are shown here. As a reference, NODA results are also included.

8.1.2. ROC and AUC

To strengthen how skillful are the different simulations performed by the 3DVar and the EnKF, the Receiver Operating Characteristic (ROC) curve is used. The probability of exceeding a given threshold is computed and verified against dichotomous observations. The ROC curve is computed as follows: the model variable is interpolated to the observation locations and if the model variable exceeds a given threshold, that model grid point is assigned a value of 1. On the contrary, if the model value does not exceed that threshold, the assigned value is 0. The same method is applied for the observations. Then, using these dichotomous values, the Hit Rate and False Alarm scores are computed. This process is repeated, varying the threshold value. Gathering the Hit Rate and False Alarm scores for the different thresholds, we obtain the ROC curve. For the 3DVar, we get the Hit Rate and False Alarm scores by simply interpolating the model values to the observation locations and apply the threshold criteria explained above. In the case of the EnKF, the ensemble mean is used as the field to be interpolated to the observation

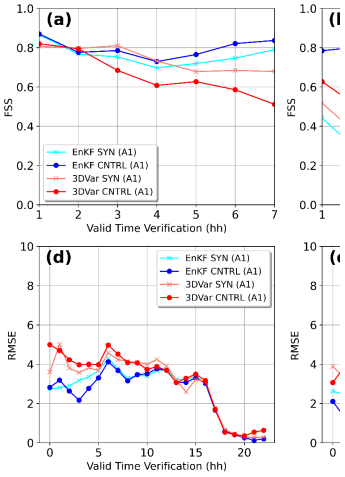

Eliminado:
Eliminado: 7
Eliminado: for NODA, 3DVar and EnKF
Eliminado:
Eliminado: (a)
Eliminado: (b)
Eliminado: (c)
Eliminado: , using a threshold
Eliminado: 1
Eliminado: .
Eliminado: Panels on the thrid row shows the
Eliminado: Lower panels: E
Eliminado: e
Eliminado: (d) R1, (e) R2 and (f) R3
Eliminado: In addition to the FSS, we also compute t... [17]
Eliminado: For 3DVar, RMSE is computed from the... [18]
Eliminado:
Eliminado: Overall
Eliminado: In general, the EnKF
Eliminado: exhibits lower (better)
Eliminado: provides the lowest (best) RMSE scores
Eliminado: compared to 3DVar, indicating improved... [19]
Eliminado: , with respect to 3DVar.
Eliminado: Additionally
Eliminado: Also,
Eliminado: it is worth
Eliminado: not
Eliminado: ing
Eliminado: e that the impact of the assimilation of... [20]
Eliminado: diminishes after approximately
Eliminado: does not last more than 4-6 hours,
Eliminado: which is consistent with findings from previous
Eliminado: in accordance with past studies.

locations. The area under the ROC curve (AUC), which measures the ability of the system to discriminate between the occurrence or nonoccurrence of the event, is also computed.

For the sake of brevity and because the results from the three sub-regions are similar, the ROC curve and AUC are computed, accounting for all the observations within the inner domain. Specifically, to compute the ROC curves, we use the 3-hour (from 00 UTC - 03 UTC 15 Oct) and 6-hour (from 00 UTC - 06 UTC 15 Oct) accumulated precipitation fields from the model simulation and the observed values registered by the rain gauges, using 1 mm and 10 mm as thresholds (Fig. 9).

Overall, DA experiments outperform the NODA runs for both the 3-hour and 6-hour accumulated precipitations, as shown by higher ROC curves and larger AUC values. Among the DA approaches, the EnKF consistently outperforms 3DVar, with greater benefits observed at the 10 mm threshold (i.e., bottom row of Fig. 9). This improvement highlights the advantages of radar reflectivity assimilation within an ensemble-based framework, especially for more intense precipitation events. To better understand this result, we closely analysed the 1-h and 6-h accumulated precipitation fields obtained from the EnKF (CNTRL) and the 3DVar (CNTRL) comparing them against corresponding observations.(see Fig. A1 and Fig. A2 in the Appendix). The 1-h accumulated precipitation (Fig. A1) shows that the EnKF localizes with high accuracy the regions where the most intense precipitation was observed, that is near Tuscany and northern Italy. Also, 3DVar correctly reproduces the rainfall in the regions affected by observed precipitation, although the maximum amounts are centered over Liguria, instead of near Tuscany. In addition, the 3DVar is also showing a tongue area of weak precipitation from Liguria to northern Italy, that does not fit with the observations. Consequently, while small differences exist between 3DVar and EnKF in the 1-h accumulated precipitation field, the low magnitude of accumulated precipitation values leads to no substantial differences in ROC verification scores. However, in the case of the 6-h accumulated precipitation (Fig. A2), the 3DVar overestimates accumulated precipitation near Liguria, Tuscany and northern Italy than the observed ones. Moreover, 3DVar is also misplacing the locations of the precipitation for some places. On the contrary, the EnKF locates with enough accuracy the regions where the accumulated precipitation was actually observed and properly estimates the observed intensity. Consequently, ROC curve for the 6-hour accumulated precipitation obtained from the EnKF produced a much better score than the 3DVar. We hypothesize that this difference could be associated with the static/climatological background error covariance matrix used by the 3DVar. Because of the fast changes in the flow associated with the IOP13 case, using a climatological background error covariance could not be as good as using a flow-dependent background error covariance matrix, which is used in the EnKF.

Eliminado: To strengthen how skillful are the different simulations performed by the 3DVar and the EnKF, the *Receiver Operating Characteristic* (ROC) curve is used. The probability of exceeding a given threshold is computed and verified against dichotomous observations. The ROC curve is computed as follows: the model variable is interpolated to the observation locations and if the model variable exceeds a given threshold, that model grid point is assigned a value of 1. On the contrary, if the model value does not exceed that threshold, the assigned value is 0. The same method is applied for the observations. Then, using these dichotomous values, the Hit Rate and False Alarm scores are computed. This process is repeated, varying the threshold value. Gathering the Hit Rate and False Alarm scores for the different thresholds, we obtain the ROC curve. For the 3DVar, we get the Hit Rate and False Alarm scores by simply interpolating the model values to the observation locations and apply the threshold criteria explained above. In the case of the EnKF, the ensemble mean is used as the field to be interpolated to the observation locations. The area under the ROC curve (AUC), which measures the ability of the system to discriminate between the occurrence or nonoccurence of the event, is also computed.

Eliminado: ¶

Eliminado: For the sake of brevity and because the results from the three sub-regions are similar, the ROC and the area under the ROC curve are computed, accounting for all the observations within the inner numerical domain. Specifically, to compute the ROC curves, we use the 3-hour (from 00 UTC - 03 UTC 15 Oct) and 6-hour (from 00 UTC - 06 UTC 15 Oct) accumulated precipitation fields from the numerical model and the observed values registered by the rain gauges, using 1 mm and 10 mm as thresholds (Fig. 9).

Eliminado: ¶

Eliminado: Results show that EnKF clearly outperforms 3DVar for the different accumulated precipitation rates and thresholds, depicting larger values of AUCs. An even bigger improvement is obtained using a larger threshold (i.e., bottom row of Fig. 9) for EnKF, where the benefits of assimilating radar observations are noticeable, in comparison with 3DVar. To better understand this result, we inspected in more detail the 1-h and 6-h accumulated precipitation fields obtained from the EnKF (CNTRL) and the 3DVar (CNTRL) and we compared those fields against the corresponding observations (see Fig. A1 in the Appendix). The 1-h accumulated precipitation (first row, Fig. A1) shows that the EnKF is localizing with high accuracy the regions where the most intense precipitation was observed, that is near Tuscany and northern Italy. Also, 3DVar correctly reproduces the rainfall in the regions affected by observed precipitation, although the maximum amounts are centered over Liguria, instead of near Tuscany. In addition, the 3DVar is also showing a tongue area of weak precipitation from Liguria to northern Italy, that does not fit with the observations. Hence, although there are some differences between 3DVar and EnKF for the 1-h accumulated precipitation field, because the accumulated precipitation values are small, the ROC verification scores from the EnKF and 3DVar do not differ significantly. However, in the case of the 6-h accumulated precipitation (second row, Fig. A1), the 3DVar produces higher values of accumulated precipitation near Liguria, Tuscany and northern Italy than the observed ones. Moreover, 3DVar is also misplacing the locations of the precipitation for some places. On the contrary, the EnKF can (a) locate with enough accuracy the regions where the accumulated precipitat ... [21]

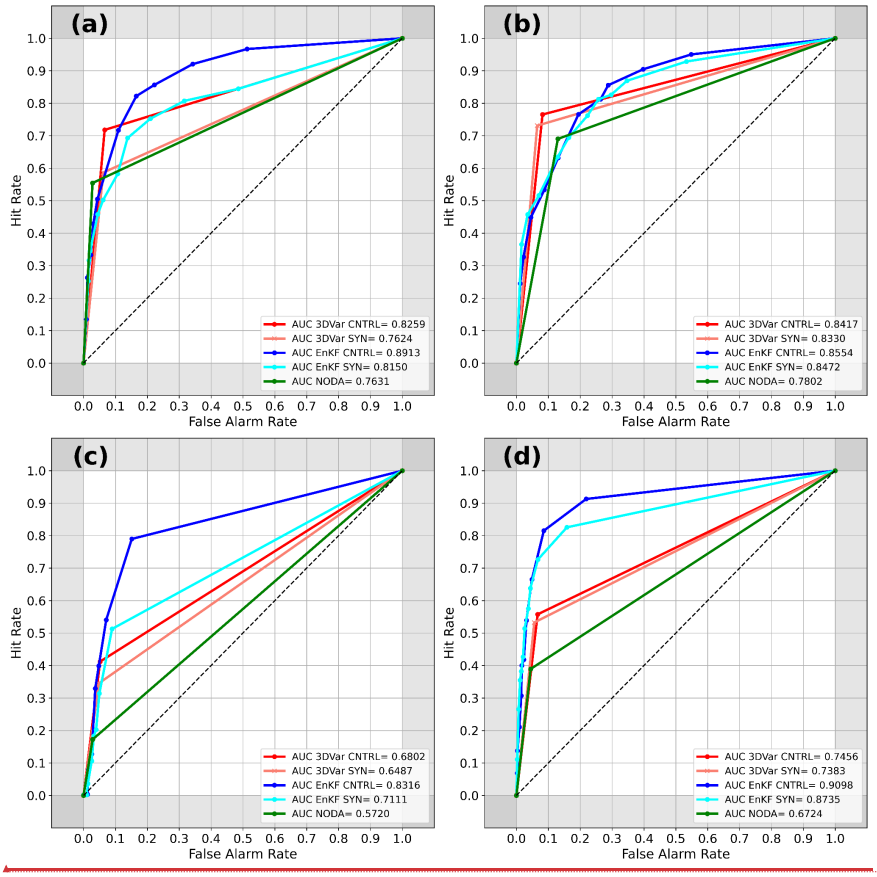

Figure 9. ROC curves and AUC associated with the 3DVar (red and pink colors) EnKF (blue and cyan colors) and NODA (green color) for the 3-hour accumulated precipitation using (a) 1 mm and (b) 10 mm threshold and 6-hour accumulated precipitation using (c) 1 mm and (d) 10 mm threshold, computed over the entire inner domain.

8.1.3. Taylor Diagrams

To strengthen the comparison of the DA schemes, the Taylor Diagram is used. This tool provides us additional information about the skill of each ensemble member in the EnKF. Here, we compute the Taylor diagram for the 6-hour and 24-hour accumulated precipitation fields, which represents the forecast ranges where the observations assimilated have more impact. Overall, results show that the NODA experiment generally exhibits the lowest correlation and largest discrepancy in standard deviation relative to observations, emphasizing that DA significantly improves the representation of precipitation fields, especially for high-impact weather events. Among the different DA approaches, the 3DVar and the EnKF ensemble mean provide comparable results, with

Con formato: Fuente: Negrita

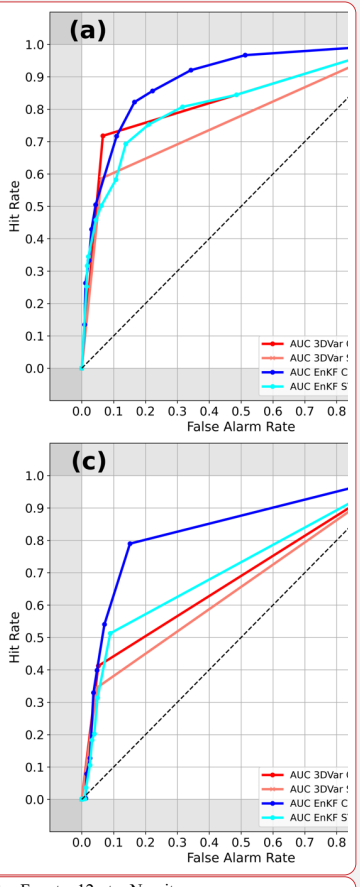

Eliminado:

Con formato: Fuente: 12 pto, Negrita

correlations ranging from approximately 0.50 to 0.61, similar RMSE and standard deviation that are symmetrically distributed around the observed reference. Notably, 3DVar tends to overestimate the standard deviation, while the EnKF ensemble mean tends to underestimate it (Fig. 10). A key advantage of EnKF lies in its individual ensemble members, some of which exhibit better performance than the 3DVar run. Although the mean difference between EnKF and 3DVar is small, the ensemble-based approach provides additional insight through its member-by-member variability. Specifically, ensemble members using the Grell-Freitas cumulus parameterization coupled with the Yonsei University planetary boundary layer scheme exhibit higher correlation and standard deviations similar to the observations in this study. Conversely, ensemble members associated with the lower scores are those using Kain-Fritsch for the cumulus parameterization and the Mellor-Yamada-Janjic for the planetary boundary layer scheme. These findings underscore the potential of multi-physics ensembles to capture diverse physical representations of convective processes, thereby enhancing forecast accuracy.

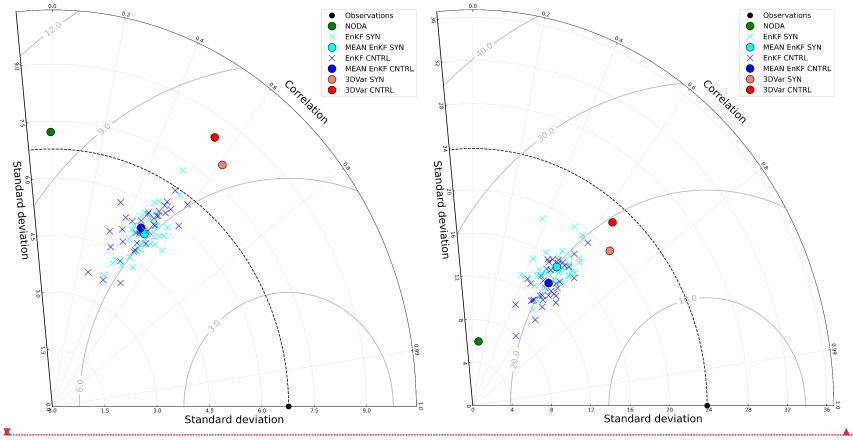

Figure 10. Taylor diagram comparing the performance of 3DVar (red) EnKF (blue) and NODA (green) for the 6-hour (left panel) and 24-hour (right panel) accumulated precipitation, valid at 06 UTC 15 October 2012.

8.2. Statistical analysis: Qendresa event

Typically, two key factors are investigated for Tropical cyclone forecasts: (a) the intensity and (b) the trajectory followed by the cyclone. Therefore, to assess the impact of assimilating both in-situ conventional and remote RSAMV observations using the 3DVar and the EnKF, these two factors are considered.

Con formato: Fuente: Negrita
Con formato: Fuente: Negrita
Eliminado: To strengthen the comparison of the D... [22]
Con formato: Fuente: Negrita
Con formato: Espacio Antes: 0 pto
Con formato: Fuente: 12 pto, Negrita

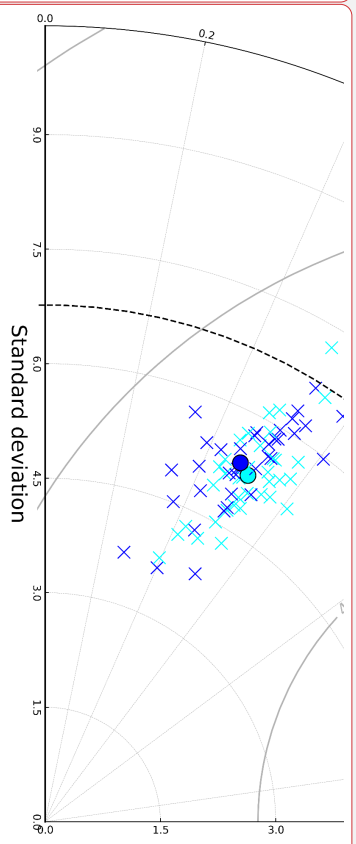

Eliminado:
Con formato: Fuente: Negrita
Con formato: Fuente: Negrita
Eliminado: performed by
Eliminado: the
Eliminado: s
Eliminado: and
Con formato: Fuente: 12 pto, Negrita
Con formato: Fuente: 12 pto, Negrita
Con formato: Fuente: 12 pto, Negrita
Con formato: Fuente: 12 pto, Negrita
Con formato: Fuente: 12 pto, Negrita
Eliminado: s
Con formato: Fuente: 12 pto, Negrita
Con formato: Fuente: 12 pto, Negrita
Con formato: Fuente: 12 pto, Negrita
Con formato: Fuente: 12 pto, Negrita
Con formato: Fuente: 12 pto, Negrita
Con formato: Fuente: 12 pto, Negrita
Con formato: Fuente: 12 pto, Negrita
Con formato: Fuente: 12 pto, Negrita
Con formato ... [23]
Con formato: Fuente: 12 pto, Negrita
Con formato: Fuente: Negrita
Con formato: Fuente: Negrita, Sin Cursiva
Con formato: Fuente: Negrita
Con formato: Fuente: Negrita
Con formato: Fuente: Negrita

8.2.1. Whisker Diagrams

For this event, the lack of in-situ observations over maritime regions poses a main challenge to properly verify the triggering and intensification of cyclones. Fortunately, the Qendresa medicane crossed just over Malta island, where a pressure drop greater than 20 hPa in 6 h, was registered by METAR at Malta airport, reaching a minimum of surface pressure of 985 hPa. Therefore, this METAR is used to quantitatively assess the skill of the different DA simulations. To compare the surface pressure registered at Malta with the different simulations, the full cyclone trajectory is used, and the grid point closest to Malta airport is selected. Specifically, the surface pressure time series measured by METAR is compared with the different DA simulations from 3DVar and EnKF, such as the 3DVar_SYN, 3DVar_CNTRL, EnKF_SYN, and the EnKF_CNTRL (Fig. 11).

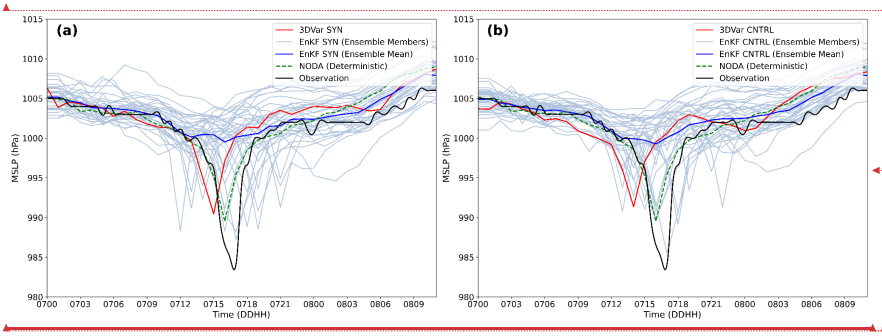

Figure 11. Temporal surface pressure evolution at the closes grid point to Malta for the (a) SYN and (b) CNTRL experiments associated with the EnKF (blue), 3DVar (red) and NODA (green), compared to the observed surface pressure registered by METARs in Malta's airport (black line).

Overall, results indicate that NODA simulation captures the timing of the observed pressure drop more accurately than the DA runs, suggesting that the large-scale dynamics are adequately represented even without data assimilation (Fig. 11). However, NODA underestimates the intensity of the medicane's central pressure.

Among the DA simulations, assimilating in-situ conventional observations enables some EnKF ensemble members to outperform NODA in both timing and intensity, whereas 3DVar shows limitations in capturing the event timing and central pressure depth (Fig. 11a). Additionally, the ensemble mean of the EnKF_SYN accurately fits the observations during the first hours of the forecast, from 00 UTC to 13 UTC 7 November (Fig. 11a), performing slightly better than 3DVAR_SYN. However, during the intensification phase, the ensemble mean of the EnKF_SYN

Con formato: Fuente: Negrita
Con formato: Fuente: Negrita
Con formato: Fuente: Negrita
Con formato: Fuente: Negrita
Con formato: Fuente: Negrita, Sin Cursiva
Con formato: Fuente: Negrita
Con formato: Fuente: Negrita
Con formato: Fuente: Negrita
Con formato: Espacio Antes: 0 pto
Con formato: Fuente: 13 pto, Negrita, Color de fuente: Azul
Con formato: Fuente: 13 pto, Negrita, Color de fuente: Azul
Eliminado:
Con formato: Fuente: 13 pto, Negrita, Color de fuente: Azul
Eliminado: lines
Con formato: Fuente: 13 pto, Negrita, Color de fuente: Azul
Eliminado: and
Con formato: Fuente: 13 pto, Negrita, Color de fuente: Azul
Con formato: Fuente: 13 pto, Negrita, Color de fuente: Azul
Eliminado: lines
Con formato: Fuente: 13 pto, Negrita, Color de fuente: Azul
Con formato: Fuente: 13 pto, Negrita, Color de fuente: Azul
Con formato: Fuente: 13 pto, Negrita, Color de fuente: Azul
Con formato: Fuente: 13 pto, Negrita, Color de fuente: Azul
Con formato: Fuente: 13 pto, Negrita, Color de fuente: Azul
Con formato: Fuente: 13 pto, Negrita, Color de fuente: Azul
Con formato: Fuente: 13 pto, Negrita, Color de fuente: Azul
Con formato: Fuente: 13 pto, Negrita, Color de fuente: Azul
Con formato: Fuente: 13 pto, Negrita, Color de fuente: Azul
Con formato: Fuente: 13 pto, Negrita, Color de fuente: Azul
Con formato: Fuente: 13 pto, Negrita, Color de fuente: Azul

barely shows the intensification of Qendresa, reaching minimum MSLP values of 1002 hPa. On the contrary, the 3DVar_SYN simulation depicts the intensification of the medicane, by deepening the MSLP and reaching values of 992 hPa, although a time shift of 3 hours is found (i.e., 15 UTC 7 November) (Fig. 11a). Finally, during the dissipation phase of Qendresa, the ensemble mean of EnKF SYN is performing a bit better than the 3DVar_SYN (Fig. 11a). These results highlight a notable limitation of the EnKF when applied to low-predictable weather events, such as Qendresa. The low predictability and the high sensitivity to the different physical parameterization schemes lead to a very different behavior of each ensemble member. Consequently, some members could completely fail in the prediction of the weather event. In this situation, our small-to-moderate ensemble will probably produce a poor flow-dependent background error covariance matrix, which is key in DA, resulting in an analysis ensemble with large spread, for which then ensemble mean will be smoothed out significantly. On the other hand, a climatological/static background error covariance matrix, like the one used in the 3DVarcould produce better results than ensemble members, as we see in Fig. 11a where we compared the 3DVar (red line) with the EnKF ensemble mean analysis (blue line). Also, it is important to note that although the ensemble mean of the EnKF_SYN is not correctly reproducing the intensification of Qendresa, some of the ensemble members accurately reproduce the observed MSLP both in deepening and timing. This suggests that using an ensemble system, even having the above-mentioned problems, is still more useful than using only a fully deterministic system such as the 3DVar, which cannot provide information about the uncertainties of the system. Therefore, we can speculate that for extreme weather events with low numerical predictability, a better approach could be using a hybrid error covariance model, where the forecast error covariance matrix is obtained linearly combining ensemble-based covariance with static climatological error covariances (Hamill and Snyder (2000); Lorenc (2003); Clayton et al., 2013; Carrió et al., 2021). The impact of using hybrid DA to improve this kind of small-scale extreme weather events could be of great interest in the weather forecast community, although it is beyond the scope of this study. For this reason, the authors leave as future work the benefits of using hybrid error covariance models to improve the forecast of extreme weather events in the Mediterranean basin.

Then, we evaluated the impact of assimilating both in-situ conventional and RSAMV observations on the accuracy of Qendresa intensity forecast (Fig. 11b). In this case, the results of the two experiments show large similarities (Fig. 11a). In terms of the 3DVar, the MSLP signature is basically the same, without showing a clear signal of improvement or diminishing, suggesting that the assimilation of RSAMVs is not enough to significantly improve the low level relevant dynamical structures associated with the genesis and intensification of Qendresa. However, in terms of the EnKF a clear improvement for a few members is found, even if it is not affecting the mean value. Indeed, some of the ensemble members depicted an intense cyclone far from the time when it was observed (approx. at 18 UTC 7 November), were corrected reducing spurious cyclones and the deepening of at least one ensemble member close to the observed value (Fig. 11b). It can be

Con formato: Fuente: 13 pto, Negrita, Color de fuente: Azul

Con formato: Fuente: 13 pto, Negrita, Color de fuente: Azul

Con formato: Fuente: 13 pto, Negrita, Color de fuente: Azul

Con formato: Fuente: 13 pto, Negrita, Color de fuente: Azul

Con formato: Fuente: 13 pto, Negrita, Color de fuente: Azul

Con formato: Fuente: 13 pto, Negrita, Color de fuente: Azul

Con formato: Fuente: 13 pto, Negrita, Color de fuente: Azul

observed that in the EnKF_CNTRL, there are more ensemble members depicting a deep cyclone at the observed time than in the case of the EnKF_SYN, showing the benefits of assimilating RSAMVs to improve the intensification estimation of Qendresa.

To quantitatively assess the performance of NODA and the different DA experiments, we use the lagged correlation technique computed between the model MSLP signatures and the observations. This technique allows us to measure how the shape of the surface pressure evolution obtained from the different simulations fits the shape of the observed MSLP, taking also into account temporal shifting. The correlation is computed for the NODA, 3DVar, and for each ensemble member from the EnKF. These results are shown using Whisker plots (Fig. 12), where a correlation of one indicates that the specific model field has the same 'V' pressure shape evolution as the observation, and that the minimum for both is found at the same time. The results show that the NODA simulation exhibits the highest correlation values among all the simulations, reaching its maximum correlation when no time-shifting is applied. For the 3DVar_SYN, the correlation is maximum and approximately equal to one when 1-hour delay is applied to forecasts (Fig. 12a). Whiskers from EnKF_SYN show that none of the ensemble members overcomes the maximum correlation value found in 3DVar_SYN. However, when the assimilation of RSAMVs is added to the in-situ conventional observations, it is found that the maximum correlation value associated with 3DVar_CNTRL using 2h of delay applied to the forecasts, is surpassed by some of the ensemble members of the EnKF_CNTRL, when a 3 or 4 hour of delay is applied (Fig. 12b).

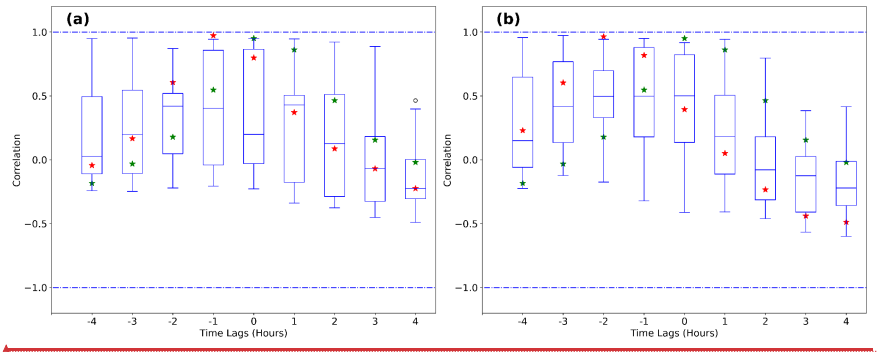

Figure 12. Whisker plots depict the lagged correlation values between the observations and the EnKF (blue boxes), the 3DVar (red stars) and NODA (green stars) for the (a) SYN and (b) CNTRL experiments. The correlation is computed considering that the observed V-shape pressure signature associated with the observations is shifted 4 hours to the left and 4 hours to the right.

Con formato: Fuente: 13 pto, Negrita, Color de fuente: Azul
Con formato: Fuente: 13 pto, Negrita, Color de fuente: Azul
Con formato: Fuente: 13 pto, Negrita, Color de fuente: Azul
Con formato: Fuente: 13 pto, Negrita, Color de fuente: Azul
Con formato: Fuente: 13 pto, Negrita, Color de fuente: Azul
Con formato: Fuente: 13 pto, Negrita, Color de fuente: Azul
Con formato: Fuente: 13 pto, Negrita, Color de fuente: Azul
Con formato: Fuente: 13 pto, Negrita, Color de fuente: Azul
Eliminado: Results from the assimilation of
Eliminado: in-situ conventional observations show that the ensemble mean of the EnKF_SYN accurately fits the observations during the first hours of the forecast, from 00 UTC to 13 UTC 7 November (Fig. 11a), performing slightly better than 3DVAR_SYN. However, during the intensification phase, the ensemble mean of the EnKF_SYN barely shows the intensification of Qen ... [24]
Eliminado: ¶
Eliminado: Then, we evaluated the impact of assim ... [25]
Eliminado: in-situ conventional and RSAMV obser ... [26]
Eliminado: ¶
Eliminado: To quantitatively assess the performan ... [27]
Eliminado: lagged correlation technique computed ... [28]
Con formato: Fuente: 13 pto, Negrita, Color de fuente: Azul
Con formato: Fuente: 13 pto, Negrita, Color de fuente: Azul
Con formato: Fuente: 13 pto, Negrita, Color de fuente: Azul
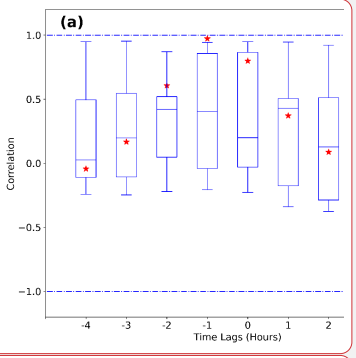

Eliminado:
Con formato: Fuente: 13 pto, Negrita, Color de fuente: Azul
Con formato: Fuente: 13 pto, Negrita, Color de fuente: Azul
Con formato: Fuente: 13 pto, Negrita, Color de fuente: Azul
Eliminado: and
Con formato: Fuente: 13 pto, Negrita, Color de fuente: Azul
Con formato: Fuente: 13 pto, Negrita, Color de fuente: Azul
Con formato: Fuente: 13 pto, Negrita, Color de fuente: Azul
Con formato: Fuente: 13 pto, Negrita, Color de fuente: Azul
Con formato: Fuente: 13 pto, Negrita, Color de fuente: Azul

8.2.2. Probability Distribution of Cyclone Center Occurrence

Due to the difficulty to accurately predict the observed trajectory of Qendresa (Pytharoulis et al., 2018), the impact of assimilating different kinds of observations on the trajectory of the medicane is investigated.

Results indicate that the NODA simulation fails to accurately capture the track of Qendresa, especially its recurvature towards Sicily after leaving Malta, as evidenced by satellite imagery. In contrast, the 3DVar_SYN accurately captures the track of Qendresa during the first hours (Fig. 13b). However, after Qendresa leaves Malta, the trajectory simulated by 3DVar_SYN diverges from the observed track, shifting north-eastwards and failing to capture the track-loop observed in satellite imagery. To quantify the benefits of assimilating in-situ conventional observations using the 3DVar or the EnKF, the probability of occurrence of a cyclone following the track observed via satellite imagery is computed. For instance, 3DVar_SYN underestimates the probability of cyclone occurrence east of Sicily, where Qendresa made landfall while looping (Fig. 13b)On the other hand, some EnKF_SYN ensemble members show a cyclone trajectory shifted significantly southward, while others reproduce the loop trajectory missed by deterministic numerical weather models (Fig. 13a). In addition, the probability of Qendresa occurrence eastwards Sicily, is in this case larger than 3DVar_SYN, showing the benefits of using the EnKF against the 3DVar (Fig. 13a). Moreover, the EnKF_SYN ensemble trajectories, in general, follow a 'V' shape (i.e., first moving towards the southeast, then moving to the east and finally moving towards the northeast) similar to the trajectory observed via satellite imagery. Although the shape of most of the EnKF_SYN trajectories agree with the observations, a southeastward displacement is evident in their location.

If both in-situ conventional and RSAMV observations are assimilated, some of the ensemble members from the EnKF_CNTRL show more accurate trajectories in comparison with EnKF_SYN: the loop trajectory is closer to the observed region of eastern Sicily (Fig. 13c). An improvement of the 3DVar_CNTRL trajectory by increasing the probability of cyclone occurrence following the observed track is observed, especially eastern of Sicily. However, 3DVar experiments are not able to reproduce the looping trajectory observed via satellite imagery (Fig. 13b-d). Hence, EnKF outperforms 3DVar showing some of the ensemble members depicting a loop trajectory, although shifted southwards and producing a probability of cyclone occurrence lower than the 3DVAR ones.

Both the EnKF and the 3DVar still have difficulties in depicting accurately the track observed by Qendresa, even after the assimilation of in-situ conventional and RSAMV observations. Because RSAMVs are useful in describing dynamical features on the upper levels of the atmosphere, we hypothesize that ingesting them via DA may not be sufficient to correct key low-level dynamical features. In this case, the assimilation of surface wind observations may help to even improve these results. However, this is beyond the scope of this study and the authors leave this

Con formato: Fuente: 13 pto, Color de fuente: Azul
Con formato: Fuente: 13 pto, Color de fuente: Azul
Con formato: Fuente: 13 pto, Color de fuente: Azul
Con formato: Fuente: 13 pto, Negrita, Color de fuente: Azul
Con formato: Fuente: 13 pto, Negrita, Color de fuente: Azul
Con formato: Fuente: 13 pto, Negrita, Color de fuente: Azul
Eliminado: The 3DVar_SYN
Con formato: Fuente: 13 pto, Negrita, Color de fuente: Azul
Con formato: Fuente: 13 pto, Negrita, Sin Cursiva, Color de fuente: Azul
Con formato: Fuente: 13 pto, Negrita, Color de fuente: Azul
Con formato: Fuente: 13 pto, Negrita, Color de fuente: Azul
Con formato: Fuente: 13 pto, Negrita, Color de fuente: Azul
Con formato: Fuente: 13 pto, Negrita, Sin Cursiva, Color de fuente: Azul
Con formato: Fuente: 13 pto, Negrita, Color de fuente: Azul
Con formato: Fuente: 13 pto, Negrita, Color de fuente: Azul
Con formato: Fuente: 13 pto, Negrita, Color de fuente: Azul
Con formato: Fuente: 13 pto, Negrita, Sin Cursiva, Color de fuente: Azul
Con formato: Fuente: 13 pto, Negrita, Color de fuente: Azul

question as future work, where other sources of information from satellites will be assimilated to improve low-level thermodynamic aspects of extreme weather events, such as medicanes.

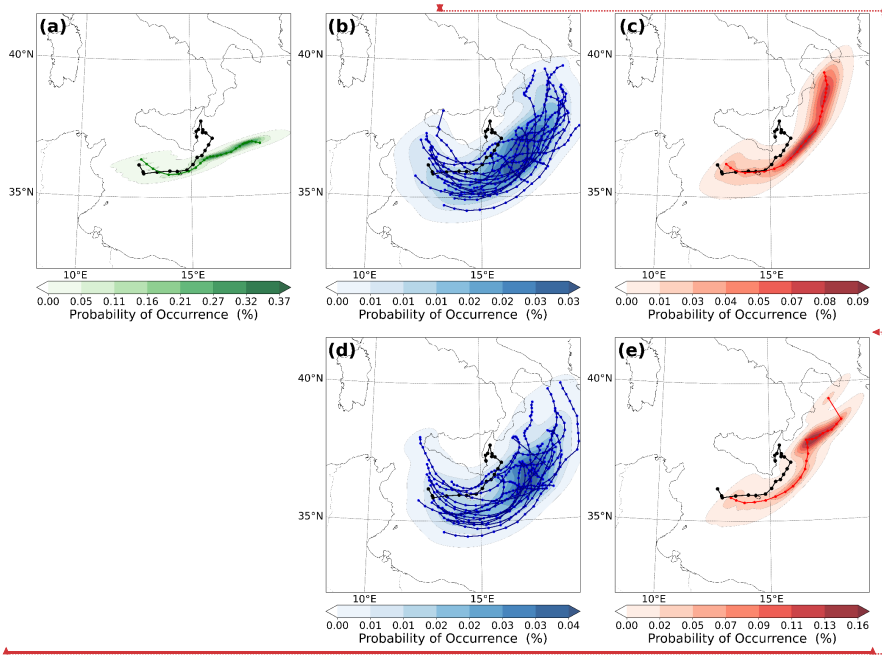

Figure 13. Probability of cyclone center occurrence computed using Gaussian KDE for (a) NODA, (b) EnKF (SYN), (c) 3DVar (SYN), (d) EnKF (CNTRL) and (e) 3DVar (CNTRL), from 11 UTC 7 November to 12 UTC 8 November 2014. Qendresa's trajectory observed via satellite imagery is depicted in black.

9. Summary and Conclusions

This study provides a quantitative assessment of the impact of two widely used DA techniques – 3DVar and EnKF – on the predictability of maritime extreme weather events. The focus is on evaluating their potential to improve forecast lead time by assimilating observations during the developing stage, as opposed to the mature stage, which affords limited time for preparedness and response. To evaluate the performance of 3DVar and EnKF we analyze two high-impact weather events triggered over the sea and later affected densely populated coastal regions. These two extreme weather events are known as (a) the high precipitation

Con formato ... [29]
Con formato ... [30]

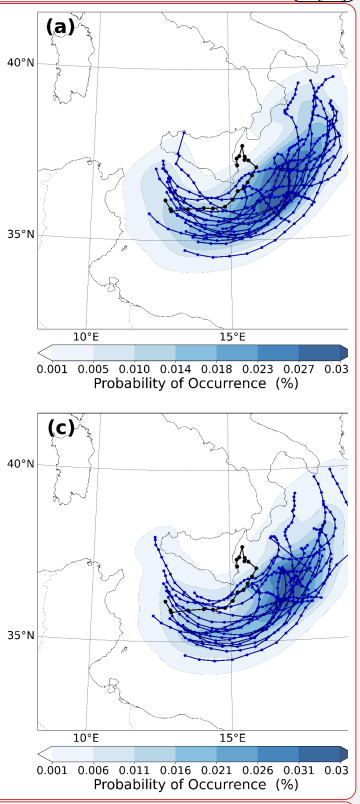

Eliminado:
Con formato ... [31]
Con formato ... [32]
Con formato ... [33]
Con formato ... [34]
Con formato ... [35]
Eliminado: b
Eliminado: c
Con formato ... [36]
Con formato ... [37]
Con formato ... [38]
Con formato ... [39]
Con formato ... [40]
Con formato ... [41]
Con formato ... [42]
Eliminado: d
Con formato ... [43]
Con formato ... [44]
Con formato ... [45]
Con formato ... [46]
Con formato ... [47]
Eliminado: In this study, we
Eliminado: ly
Eliminado: high-resolution
Con formato ... [48]
Con formato ... [49]
Con formato ... [50]
Con formato ... [51]
Con formato ... [52]
Con formato ... [53]
Con formato ... [54]
Con formato ... [55]
Eliminado: Here, we
Con formato ... [56]
Con formato ... [57]
Con formato ... [58]

event registered during the 13th Intensive Observation Period (IOP13) affecting the western, northern and central parts of Italy, and (b) the intense Tropical-like Mediterranean Cyclone (medicane) known as Qendresa, that affected the islands of Pantelleria, Lampedusa, Malta and Sicily. These weather events pose a serious challenge for the numerical weather prediction community due to their low predictability, resulting from their initialization over the sea, where in-situ observations are sparse and initial conditions are poorly estimated. Furthermore, their evolution over complex terrain regions introduces additional forecasting challenges.

For these two extreme weather events, both 3DVar and EnKF DA methods were applied, with the type and number of assimilated observations varying based on the data availability. For Qendresa, we assimilated (a) hourly in-situ conventional observations and (b) wind speed and wind direction profiles of the entire atmosphere (RSAMVs) derived from geostationary satellites every 20-min, providing high spatial and temporal resolution observations covering the Central Mediterranean Sea, where Qendresa initiated and evolved. On the other hand, for the IOP13, we assimilated (a) hourly in-situ conventional observations and (b) 15-min 3D reflectivity observations from two type-C Doppler Weather Radars.

Because of the different thermodynamic characteristics associated with Qendresa and IOP13, a set of different verification metrics were used for each of these extreme weather events. The Filtering method (FSS and RMSE), the ROC/AUC and the Taylor diagram were used to verify the numerical simulations from 3DVar and EnKF associated with IOP13. In the case of Qendresa, we used the Whisker diagrams and the Probability Distribution of Cyclone Center Occurrence verification scores. For the IOP13, both the Filtering method and Taylor diagram verification show that EnKF slightly outperforms 3DVar, although the differences are not significant. In addition, it was observed that the assimilation of spatial and temporal high-resolution reflectivity observations significantly improved the forecast for both 3DVar and EnKF, showing the key role of this type of observation. On the other hand, the ROC and AUC scores clearly show that EnKF outperforms 3DVar. For the Qendresa event, while the ensemble mean of EnKF underestimates the intensity of the medicane compared to 3DVar, some individual EnKF ensemble members produce more accurate results than 3DVar. This behaviour suggests how important it is using an ensemble forecast system to predict extreme weather events at high spatial and temporal resolution. Regarding the cyclone's trajectory, the EnKF provides a more realistic representation of the Qendresa's observed path.

Although the EnKF technique has shown in general better performance against the 3DVar for the two extreme weather events analyzed in this study, it is also important to account for the computational resources required by each method. The 3DVar requires much less computational resources than the EnKF because it does not need to build an ensemble of considerable size, and it does not need either to simulate model trajectories between the assimilation of a set of observations at time t1 and the subsequent set of observations valid at t2. This makes the 3DVar

Con formato ... [81]
Con formato ... [82]
Eliminado: Nowadays,
Eliminado: T
Eliminado: t
Con formato ... [83]
Con formato ... [84]
Eliminado: represent
Con formato ... [85]
Con formato ... [86]
Con formato ... [87]
Con formato ... [88]
Con formato ... [89]
Con formato ... [90]
Eliminado: these convective systems evolved towar ... [91]
Con formato ... [92]
Eliminado: The two DA methods compared in this ... [93]
Eliminado: For the
Eliminado: se
Eliminado: two
Eliminado: extreme weather
Eliminado: events,
Eliminado: b
Eliminado: are
Con formato ... [94]
Con formato ... [95]
Con formato ... [96]
Con formato ... [97]
Con formato ... [98]
Con formato ... [99]
Con formato ... [100]
Eliminado: used
Eliminado: for these two extreme weather events
Eliminado: , and
Con formato ... [101]
Con formato ... [102]
Con formato ... [103]
Eliminado: was different
Eliminado: changes
Eliminado: depending
Con formato ... [104]
Con formato ... [105]
Con formato ... [106]
Con formato ... [107]
Con formato ... [108]
Con formato ... [109]
Con formato ... [110]
Con formato ... [111]
Con formato ... [112]
Con formato ... [113]
Con formato ... [114]
Con formato ... [115]
Con formato ... [116]
Con formato ... [117]
Con formato ... [118]
Con formato ... [119]
Con formato ... [120]
Eliminado: event
Eliminado: the
Con formato ... [121]
Con formato ... [122]
Con formato ... [123]
Con formato ... [124]
Con formato ... [125]

appealing because it is much faster and cheaper than the EnKF, and it makes this technique particularly suitable for operational purposes at the small weather forecast centers.

Another interesting result that we have shown in this study is that depending on the level of predictability of the weather event and its sensitivity to numerical physical parameterizations used to build the ensemble, the 3DVar performs better than the EnKF ensemble mean. We speculated that this is linked to the way the background error covariances from these two methods are built. Based on this, we suppose that a better approach could be to use Hybrid error covariance models, where the forecast error covariance matrix is obtained linearly combining the ensemble-based error covariance from the EnKF and the static climatological error covariance matrix from the 3DVar.

Further work will investigate the impact of using hybrid DA schemes in comparison to standard 3DVar or EnKF. In this scenario, it is expected that the hybrid error covariance matrix will be more precise than the one derived from the ensemble members or from climatology, which on their own are not able to reproduce key aspects of challenging extreme weather events. High temporal and spatial observations from Doppler Weather radars, such as reflectivity and radial wind velocities, will be assimilated for this case to obtain accurate analysis and thus, improve the short-range forecast of this catastrophic flash-flood event. In addition, it is important to highlight that satellite-based data assimilation provides a significant opportunity for enhancing convective-scale forecasting, particularly in data-sparse maritime regions, such as the Mediterranean, where the formation of extreme weather events like tropical-like cyclones is increasingly impacting densely populated areas. Future studies integrating high-resolution satellite observations, such as cloud top heights, thermodynamic profiles or cloud properties, could further enhance the accuracy of convective-scale predictions, improving early warning capabilities and disaster preparedness.

Acknowledgements:

The first author acknowledges the European Union's Horizon 2020 research and innovation programme under the Marie Sklodowska-Curie grant agreement 101106403 [SENTINEL]. This research is also sponsored by the Ministerio de Ciencia e Innovación-Agencia Estatal de Investigación TRAMPAS (PID2020-113036RB-I00/AEI/10.13039/501100011033). The authors thankfully acknowledge Météo-France for supplying the data and HyMeX database teams (ESPRI/IPSL and SEDOO/OMP) for their help in accessing the data. The author also acknowledges the computer resources at MareNostrum IV and CRAY supercomputers, as well as the technical support provided by the Barcelona Supercomputer Center (RES-AECT-2017-1-0014, RES-AECT-2017-2-0014) and

Con formato: Fuente: 13 pto, Negrita, Color de fuente: Azul
Con formato: Fuente: 13 pto, Negrita, Color de fuente: Azul
Eliminado: our
Con formato: Fuente: 13 pto, Negrita, Color de fuente: Azul
Con formato: Fuente: 13 pto, Negrita, Color de fuente: Azul
Eliminado: using
Con formato: Fuente: 13 pto, Negrita, Color de fuente: Azul
Con formato: Fuente: 13 pto, Negrita, Color de fuente: Azul
Con formato: Fuente: 13 pto, Negrita, Color de fuente: Azul
Con formato: Fuente: 13 pto, Negrita, Color de fuente: Azul
Eliminado: As a case study, a catastrophic and deadly flash flood event affecting the Balearic Islands will be used to quantitatively assess the skill performance of the hybrid DA scheme against the EnKF and a more advanced version of the 3DVar, which is known as the 4DVar.
Eliminado: In this case, most of the ensemble members of did not reproduce the convective cells that later r... [153]
Con formato: Fuente: 13 pto, Negrita, Color de fuente: Azul
Con formato: Fuente: 13 pto, Negrita, Color de fuente: Azul
Con formato: Fuente: 13 pto, Negrita, Color de fuente: Azul
Eliminado: properly
Con formato: Fuente: 13 pto, Negrita, Color de fuente: Azul
Con formato: Fuente: 13 pto, Negrita, Color de fuente: Azul
Eliminado: ing
Eliminado: this
Con formato: Fuente: 13 pto, Negrita, Color de fuente: Azul
Eliminado: episode
Con formato: Fuente: 13 pto, Negrita, Color de fuente: Azul
Con formato: Fuente: 13 pto, Negrita, Color de fuente: Azul
Con formato: Fuente: 13 pto, Negrita, Color de fuente: Azul
Con formato: Fuente: 13 pto, Negrita, Color de fuente: Azul
Con formato: Fuente: 13 pto, Negrita, Color de fuente: Azul
Con formato: Fuente: 13 pto, Negrita, Color de fuente: Azul
Con formato: Fuente: 13 pto, Negrita, Color de fuente: Azul
Con formato: Fuente: 13 pto, Negrita, Color de fuente: Azul
Con formato: Fuente: 13 pto, Negrita, Color de fuente: Azul
Con formato: Fuente: 13 pto, Negrita, Color de fuente: Azul
Con formato: Fuente: 13 pto, Color de fuente: Azul
Con formato: Fuente: 13 pto, Color de fuente: Azul
Con formato: Fuente: 13 pto, Color de fuente: Azul
Con formato: Fuente: 13 pto, Color de fuente: Azul
Con formato: Fuente: 13 pto, Color de fuente: Azul
Con formato: Fuente: 13 pto, Color de fuente: Azul
Con formato: Fuente: 13 pto, Color de fuente: Azul

ECMWF data center, required to perform the high-resolution simulations presented in this study.

References

Albergel, C., Zheng, Y., Bonan, B., Dutra, E., Rodríguez-Fernández, N., Munier, S., ... & Calvet, J. C. (2020). Data assimilation for continuous global assessment of severe conditions over terrestrial surfaces. Hydrology and Earth System Sciences, 24(9), 4291-4316.

Amengual, A., Carrió, D. S., Ravazzani, G., & Homar, V. (2017). A comparison of ensemble strategies for flash flood forecasting: The 12 october 2007 case study in Valencia, Spain. Journal of Hydrometeorology, 18(4), 1143-1166.

Amengual, A., Hermoso, A., Carrió, D. S., & Homar, V. (2021). The Sequence of Heavy Precipitation and Flash Flooding of 12 and 13 September 2019 in Eastern Spain. Part II: A Hydrometeorological Predictability Analysis Based on Convection-Permitting Ensemble Strategies. Journal of Hydrometeorology, 22(8), 2153-2177.

Anderson, J. L., & Anderson, S. L. (1999). A Monte Carlo implementation of the nonlinear filtering problem to produce ensemble assimilations and forecasts. Monthly weather review, 127(12), 2741-2758.

Anderson, J. L. (2001). An ensemble adjustment Kalman filter for data assimilation. Monthly weather review, 129(12), 2884-2903.

Anderson, J. L., & Collins, N. (2007). Scalable implementations of ensemble filter algorithms for data assimilation. Journal of Atmospheric and Oceanic Technology, 24(8), 1452-1463.

Anderson, J., Hoar, T., Raeder, K., Liu, H., Collins, N., Torn, R., & Avellano, A. (2009). The data assimilation research testbed: A community facility. Bulletin of the American Meteorological Society, 90(9), 1283-1296.

Ballard, Susan P., et al. "Performance of 4D-Var NWP-based nowcasting of precipitation at the Met Office for summer 2012." Quarterly Journal of the Royal Meteorological Society 142.694 (2016): 472-487.

Con formato ... [154]
Eliminado: The first author acknowledges the
Eliminado: Ministerio de Universidades (Plan de ... [155]
Con formato ... [156]
Con formato ... [157]
Con formato ... [158]
Con formato ... [159]
Con formato ... [160]
Con formato ... [161]
Con formato ... [162]
Con formato ... [163]
Con formato ... [164]
Con formato ... [165]
Con formato ... [166]
Con formato ... [167]
Con formato ... [168]
Con formato ... [169]
Con formato ... [170]
Con formato ... [171]
Con formato ... [172]
Con formato ... [173]
Con formato ... [174]
Con formato ... [175]
Con formato ... [176]
Con formato ... [177]
Con formato ... [178]
Con formato ... [179]
Con formato ... [180]
Con formato ... [181]
Con formato ... [182]
Con formato ... [183]
Con formato ... [184]
Con formato ... [185]
Con formato ... [186]
Con formato ... [187]
Con formato ... [188]
Con formato ... [189]
Con formato ... [190]
Con formato ... [191]
Con formato ... [192]
Con formato ... [193]
Con formato ... [194]
Con formato ... [195]
Con formato ... [196]
Con formato ... [197]
Con formato ... [198]
Con formato ... [199]

Barker DM, Huang W, Guo Y-R, Bourgeois A, Xiao XN (2004) A three-dimensional variational data assimilation system for MM5: implementation and initial results. Mon Wea Rev 132:897–914

Bowman, A. W., & Azzalini, A. (1997). Applied smoothing techniques for data analysis: the kernel approach with S-Plus illustrations (Vol. 18). OUP Oxford.

Bryan, G. H., & Rotunno, R. (2005, October). Statistical convergence in simulated moist absolutely unstable layers. In Preprints, 11th Conf. on Mesoscale Processes, Albuquerque, NM, Amer. Meteor. Soc. M (Vol. 1).

Capecchi V, Antonini A, Benedetti R, Fibbi L, Melani S, Rovai L, Ricchi A, Cerrai D. Assimilating X- and S-Band Radar Data for a Heavy Precipitation Event in Italy. Water. 2021; 13(13):1727. https://doi.org/10.3390/w13131727.

Carrassi, A., Bocquet, M., Bertino, L., & Evensen, G. (2018). Data assimilation in the geosciences: An overview of methods, issues, and perspectives. *Wiley Interdisciplinary Reviews: Climate Change*, *9*(5), e535.

Carrió, D. S., & Homar, V. (2016). Potential of sequential EnKF for the short-range prediction of a maritime severe weather event. Atmospheric Research, 178, 426-444.

Carrió, D. S., Homar, V., Jansa, A., Romero, R., & Picornell, M. A. (2017). Tropicalization process of the 7 November 2014 Mediterranean cyclone: Numerical sensitivity study. Atmospheric Research, 197, 300-312.

Carrió, D. S., Homar, V., & Wheatley, D. M. (2019). Potential of an EnKF storm-scale data assimilation system over sparse observation regions with complex orography. Atmospheric Research, 216, 186-206.

Carrió, D. S., Bishop, C. H., & Kotsuki, S. (2021). Empirical determination of the covariance of forecast errors: An empirical justification and reformulation of hybrid covariance models. Quarterly Journal of the Royal Meteorological Society, 147(736), 2033-2052.

Carrió, D. S., Jansà, A., Homar, V., Romero, R., Rigo, T., Ramis, C., ... & Maimó, A. (2022). Exploring the benefits of a Hi-EnKF system to forecast an extreme weather event. The 9th October 2018 catastrophic flash flood in Mallorca. Atmospheric Research, 265, 105917.

Carrió, D. S. (2023): Improving the predictability of the Qendresa Medicane by the assimilation of conventional and atmospheric motion vector observations. Storm-scale analysis and short-range forecast, Nat. Hazards Earth Syst. Sci. Discuss. https://doi.org/10.5194/nhess-2022-58,

Cioni, G, Cerrai, D, Klocke, D. (2018). Investigating the predictability of a Mediterranean tropical-like cyclone using a storm-resolving model. Q J R Meteorol Soc.; 144: 1598– 1610. https://doi.org/10.1002/qj.3322

Clayton, A. M., Lorenc, A. C., & Barker, D. M. (2013). Operational implementation of a hybrid ensemble/4D-Var global data assimilation system at the Met Office. Quarterly Journal of the Royal Meteorological Society, 139(675), 1445-1461.

Con formato: Fuente: Cursiva, Color de fuente: Azul, Resaltar

Con formato: Justificado, Interlineado: sencillo

Con formato: Interlineado: sencillo

Con formato: Sin Resaltar

Corrales, P. B., Galligani, V., Ruiz, J., Sapucci, L., Dillon, M. E., Skabar, Y. G., ... & Nesbitt, S. W. (2023). Hourly assimilation of different sources of observations including satellite radiances in a mesoscale convective system case during RELAMPAGO campaign. Atmospheric Research, 281, 106456.

Courtier, P. H. I. L. I. P. P. E., Thépaut, J. N., & Hollingsworth, A. (1994). A strategy for operational implementation of 4D-Var, using an incremental approach. Quarterly Journal of the Royal Meteorological Society, 120(519), 1367-1387.

Di Muzio, E, Riemer, M, Fink, AH, Maier-Gerber, M. Assessing the predictability of Medicanes in ECMWF ensemble forecasts using an object-based approach. Q J R Meteorol Soc. 2019; 145: 1202–1217. https://doi.org/10.1002/qj.3489

Dowell, D. C., Wicker, L. J., & Snyder, C. (2011). Ensemble Kalman filter assimilation of radar observations of the 8 May 2003 Oklahoma City supercell: Influences of reflectivity observations on storm-scale analyses. Monthly Weather Review, 139(1), 272-294.

Drobinski, P., Ducrocq, V., Alpert, P., Anagnostou, E., Béranger, K., Borga, M., ... & Wernli, H. (2014). HyMeX: A 10-year multidisciplinary program on the Mediterranean water cycle. Bulletin of the American Meteorological Society, 95(7), 1063-1082.

Dudhia, J. (1989). Numerical study of convection observed during the winter monsoon experiment using a mesoscale two-dimensional model. Journal of Atmospheric Sciences, 46(20), 3077-3107.

Eliassen, A. (1954). Provisional report on calcuation of spatial covariance and autocorrelation of the pressure field. Peport no 5, Videnskaps-Akademiets Institutt for Vaer-Og Klimaforskning, Oslo, Norway, 12.

Emanuel, K. (2005). Genesis and maintenance of" Mediterranean hurricanes". Advances in Geosciences, 2, 217-220.

Evensen, G. (1994). Sequential data assimilation with a nonlinear quasi-geostrophic model using Monte Carlo methods to forecast error statistics. Journal of Geophysical Research: Oceans, 99(C5), 10143-10162.

Federico, S., Torcasio, R. C., Puca, S., Vulpiani, G., Comellas Prat, A., Dietrich, S., & Avolio, E. (2021). Impact of radar reflectivity and lightning data assimilation on the rainfall forecast and predictability of a summer convective thunderstorm in Southern Italy. Atmosphere, 12(8), 958.

Ferrer Hernández, A. L., González Jardines, P. M., Sierra Lorenzo, M., & de la Caridad Aguiar Figueroa, D. (2022). Impact of the Assimilation of Non-Precipitating Echoes Reflectivity Data on the Short-Term Numerical Forecast of SisPI. Environmental Sciences Proceedings, 19(1), 13.

Ferretti, R., Pichelli, E., Gentile, S., Maiello, I., Cimini, D., Davolio, S., ... & Rotunno, R. (2014). Overview of the first HyMeX Special Observation Period over Italy: observations and model results. Hydrology and Earth System Sciences, 18(5), 1953-1977.

Con formato: Fuente: Cursiva, Color de fuente: Azul, Resaltar

Con formato: Interlineado: sencillo

Con formato: Fuente: Cursiva, Color de fuente: Azul, Resaltar

Con formato: Interlineado: sencillo

Fitzpatrick, P. J., Li, Y., Hill, C., Karan, H., Lim, E., & Xiao, Q. (2007, June). The impact of radar data assimilation on a squall line in Mississippi. In 22nd Conference on Weather Analysis and Forecasting/18th Conference on Numerical Weather Prediction.

Flaounas, E., Lagouvardos, K., Kotroni, V., Claud, C., Delanoë, J., Flamant, C., ... & Wernli, H. (2016). Processes leading to heavy precipitation associated with two Mediterranean cyclones observed during the HyMeX SOP1. *Quarterly Journal of the Royal Meteorological Society*, *142*, 275-286.

Fujita, T., Stensrud, D. J., & Dowell, D. C. (2007). Surface data assimilation using an ensemble Kalman filter approach with initial condition and model physics uncertainties. Monthly weather review, 135(5), 1846-1868.

Gao, J., Fu, C., Stensrud, D. J., & Kain, J. S. (2016). OSSEs for an ensemble 3DVAR data assimilation system with radar observations of convective storms. Journal of the Atmospheric Sciences, 73(6), 2403-2426.

Garcies, L., & Homar, V. (2009). Ensemble sensitivities of the real atmosphere: application to Mediterranean intense cyclones. Tellus A: Dynamic Meteorology and Oceanography, 61(3), 394-406.

Gaspari, G., & Cohn, S. E. (1999). Construction of correlation functions in two and three dimensions. Quarterly Journal of the Royal Meteorological Society, 125(554), 723-757.

Grell, G. A., & Freitas, S. R. (2014). A scale and aerosol aware stochastic convective parameterization for weather and air quality modeling. Atmospheric Chemistry and Physics, 14(10), 5233-5250.

Gustafsson, N., Janjić, T., Schraff, C., Leuenberger, D., Weissmann, M., Reich, H., ... & Fujita, T. (2018). Survey of data assimilation methods for convective-scale numerical weather prediction at operational centres. Quarterly Journal of the Royal Meteorological Society, 144(713), 1218-1256.

Hacker, J. P., Anderson, J. L., & Pagowski, M. (2007). Improved vertical covariance estimates for ensemble-filter assimilation of near-surface observations. Monthly Weather Review, 135(3), 1021-1036.

Hamill, T. M., & Snyder, C. (2000). A hybrid ensemble Kalman filter–3D variational analysis scheme. Monthly Weather Review, 128(8), 2905-2919.

Honda, T., Miyoshi, T., Lien, G. Y., Nishizawa, S., Yoshida, R., Adachi, S. A., ... & Bessho, K. (2018). Assimilating all-sky Himawari-8 satellite infrared radiances: A case of Typhoon Soudelor (2015). Monthly Weather Review, 146(1), 213-229.

Hong, S. Y., Noh, Y., & Dudhia, J. (2006). A new vertical diffusion package with an explicit treatment of entrainment processes. Monthly weather review, 134(9), 2318-2341.

Houtekamer, P. L., & Mitchell, H. L. (1998). Data assimilation using an ensemble Kalman filter technique. Monthly Weather Review, 126(3), 796-811.

Con formato: Fuente: Cursiva, Color de fuente: Azul, Resaltar

Con formato: Interlineado: sencillo

Hu, Junjun, et al. "Assessment of Storm-Scale Real Time Assimilation of GOES-16 GLM Lightning-Derived Water Vapor Mass on Short Term Precipitation Forecasts During the 2020 Spring Forecast Experiment." Journal of Geophysical Research: Atmospheres 126.21 (2021): e2021JD034603.

Huang, X. Y., Xiao, Q., Barker, D. M., Zhang, X., Michalakes, J., Huang, W., ... & Kuo, Y. H. (2009). Four-dimensional variational data assimilation for WRF: Formulation and preliminary results. Monthly Weather Review, 137(1), 299-314.

Hung MK, Tien DD, Quan DD, Duc TA, Dung PTP, Hole LR, Nam HG. Assessments of Use of Blended Radar–Numerical Weather Prediction Product in Short-Range Warning of Intense Rainstorms in Localized Systems (SWIRLS) for Quantitative Precipitation Forecast of Tropical Cyclone Landfall on Vietnam's Coast. Atmosphere. 2023; 14(8):1201. https://doi.org/10.3390/atmos14081201

Iacono, M. J., Delamere, J. S., Mlawer, E. J., Shephard, M. W., Clough, S. A., & Collins, W. D. (2008). Radiative forcing by long-lived greenhouse gases: Calculations with the AER radiative transfer models. Journal of Geophysical Research: Atmospheres, 113(D13).

Janjić, Z. I. (1990). The step-mountain coordinate: Physical package. Monthly weather review, 118(7), 1429-1443.

Janić, Z. I. (2001). Nonsingular implementation of the Mellor-Yamada level 2.5 scheme in the NCEP Meso model.

Janjić, Tijana, Yuefei Zeng, and Yvonne Ruckstuhl. "Weakly Constrained LETKF for Convective-Scale Data Assimilation." (2022).

Jansa, A., Alpert, P., Arbogast, P., Buzzi, A., Ivancan-Picek, B., Kotroni, V., ... & Speranza, A. (2014). MEDEX: a general overview. *Natural Hazards and Earth System Sciences*, *14*(8), 1965-1984.

Jones, T. A., Otkin, J. A., Stensrud, D. J., & Knopfmeier, K. (2013). Assimilation of satellite infrared radiances and Doppler radar observations during a cool season observing system simulation experiment. Monthly weather review, 141(10), 3273-3299.

Kain, J. S., & Fritsch, J. M. (1990). A one-dimensional entraining/detraining plume model and its application in convective parameterization. Journal of Atmospheric Sciences, 47(23), 2784-2802.

Kain, J. S. (2004). The Kain–Fritsch convective parameterization: an update. Journal of applied meteorology, 43(1), 170-181.

Kalnay, E. (2003). Atmospheric modeling, data assimilation and predictability. Cambridge university press.

Lagasio, M., Silvestro, F., Campo, L., & Parodi, A. (2019). Predictive Capability of a High-Resolution Hydrometeorological Forecasting Framework Coupling WRF Cycling 3DVAR and Continuum. Journal of Hydrometeorology, 20(7), 1307-1337. https://doi.org/10.1175/JHM-D-18-0219.1

Le Dimet, F. X., & Talagrand, O. (1986). Variational algorithms for analysis and assimilation of meteorological observations: theoretical aspects. Tellus A: Dynamic Meteorology and Oceanography, 38(2), 97-110.

Con formato: Fuente: Cursiva, Color de fuente: Azul, Resaltar

Con formato: Interlineado: sencillo

Con formato: Fuente: Cursiva, Color de fuente: Azul, Resaltar

Con formato: Interlineado: sencillo

Con formato: Fuente: Cursiva, Color de fuente: Azul, Resaltar

Con formato: Interlineado: sencillo

Con formato: Fuente: (Predeterminada) Arial, Color de fuente: Negro

Con formato: Sangría: Izquierda: 1,27 cm, Interlineado: sencillo

Lee, J. H., Lee, H. H., Choi, Y., Kim, H. W., & Lee, D. K. (2010). Radar data assimilation for the simulation of mesoscale convective systems. Advances in Atmospheric Sciences, 27, 1025-1042.

Li, X., J. Ming, M. Xue, Y. Wang, and K. Zhao, 2015: Implementation of a dynamic equation constraint based on the steady state momentum equations within the WRF hybrid ensemble-3DVar data assimilation system and test with radar T-TREC wind assimilation for tropical Cyclone Chanthu (2010). J. Geophys. Res. Atmos., 120, 4017–4039, doi: 10.1002/2014JD022706.

Li, X., Zeng, M., Wang, Y., Wang, W., Wu, H., & Mei, H. (2016). Evaluation of two momentum control variable schemes and their impact on the variational assimilation of radarwind data: Case study of a squall line. Advances in Atmospheric Sciences, 33, 1143-1157.

Lorenc, A. C. (1981). A global three-dimensional multivariate statistical interpolation scheme. Monthly Weather Review, 109(4), 701-721.

Lorenc, A. C. (1986). Analysis methods for numerical weather prediction. Quarterly Journal of the Royal Meteorological Society, 112(474), 1177-1194.

Lorenc, A. C. (2003). The potential of the ensemble Kalman filter for NWP—A comparison with 4D-Var. Quarterly Journal of the Royal Meteorological Society: A journal of the atmospheric sciences, applied meteorology and physical oceanography, 129(595), 3183-3203.

Llasat, M., & Sempere-Torres, D. (2001). Heavy rains and floods in west mediterranean areas: a climatic feature. Geophysical Research Abstr acts, 3.

Llasat, M. C., Llasat-Botija, M., Prat, M. A., Porcu, F., Price, C., Mugnai, A., ... & Nicolaides, K. (2010). High-impact floods and flash floods in Mediterranean countries: the FLASH preliminary database. Advances in Geosciences, 23, 47-55.

Mason, I., 1982: A model for assessment of weather forecasts. Aust. Met. Mag., 30, 291-303.

Mass, C. F., Ovens, D., Westrick, K., & Colle, B. A. (2002). Does increasing horizontal resolution produce more skillful forecasts?: The Results of Two Years of real-Time Numerical Weather Prediction over the Pacific Northwest. Bulletin of the American Meteorological Society, 83(3), 407-430.

Mazzarella, V.; Maiello, I.; Ferretti, R.; Capozzi, V.; Picciotti, E.; Alberoni, P.; Marzano, F.; Budillon, G. Reflectivity and velocity radar data assimilation for two flash flood events in central Italy: A comparison between 3D and 4D variational methods. Q. J. R. Meteorol. Soc. 2020, 146, 348–366.

Mazzarella, V., Ferretti, R., Picciotti, E., & Marzano, F. S. (2021). Investigating 3D and 4D variational rapid-update-cycling assimilation of weather radar reflectivity for a heavy rain event in central Italy. Natural Hazards and Earth System Sciences, 21(9), 2849-2865.

Mittermaier, M., & Roberts, N. (2010). Intercomparison of spatial forecast verification methods: Identifying skillful spatial scales using the fractions skill score. Weather and Forecasting, 25(1), 343-354.

Nakanishi, M., & Niino, H. (2006). An improved Mellor–Yamada level-3 model: Its numerical stability and application to a regional prediction of advection fog. Boundary-Layer Meteorology, 119, 397-407.

Nakanishi, M., & Niino, H. (2009). Development of an improved turbulence closure model for the atmospheric boundary layer. Journal of the Meteorological Society of Japan. Ser. II, 87(5), 895-912.

Pakalidou, N., & Karacosta, P. (2018). Study of very long-period extreme precipitation records in Thessaloniki, Greece. *Atmospheric Research*, *208*, 106-115.

Park, S. K., & Županski, D. (2003). Four-dimensional variational data assimilation for mesoscale and storm-scale applications. Meteorology and Atmospheric Physics, 82(1), 173-208.

Parrish, D., and J. Derber, 1992: The National Meteorological Center's spectral statistical-interpolation analysis system. Mon. Wea. Rev., 120, 1747–1763, doi:10.1175/1520-0493(1992)120<1747:TNMCSS>2.0.CO;2.

Petterssen, S. (1956). Weather analysis and forecasting: motion and motion systems. McGraw-Hill.

Pichelli, E., Rotunno, R. and Ferretti, R. (2017), Effects of the Alps and Apennines on forecasts for Po Valley convection in two HyMeX cases. Q.J.R. Meteorol. Soc., 143: 2420-2435. https://doi.org/10.1002/qj.3096

Poterjoy, J. (2016). A localized particle filter for high-dimensional nonlinear systems. Monthly Weather Review, 144(1), 59-76.

Pu, Z., Li, X., Velden, C. S., Aberson, S. D., & Liu, W. T. (2008). The impact of aircraft dropsonde and satellite wind data on numerical simulations of two landfalling tropical storms during the tropical cloud systems and processes experiment. Weather and Forecasting, 23(1), 62-79.

Pytharoulis, I., Matsangouras, I. T., Tegoulias, I., Kotsopoulos, S., Karacostas, T. S., & Nastos, P. T. (2017). Numerical study of the medicane of November 2014. In Perspectives on Atmospheric Sciences (pp. 115-121). Springer International Publishing.

Pytharoulis, I. (2018). Analysis of a Mediterranean tropical-like cyclone and its sensitivity to the sea surface temperatures. Atmospheric Research, 208, 167-179.

Rabier, F., Järvinen, H., Klinker, E., Mahfouf, J. F., & Simmons, A. (2000). The ECMWF operational implementation of four-dimensional variational assimilation. I: Experimental results with simplified physics. Quarterly Journal of the Royal Meteorological Society, 126(564), 1143-1170.

Rawlins, F., Ballard, S. P., Bovis, K. J., Clayton, A. M., Li, D., Inverarity, G. W., ... & Payne, T. J. (2007). The Met Office global four-dimensional variational data assimilation scheme. Quarterly Journal of the Royal Meteorological Society: A journal of the atmospheric sciences, applied meteorology and physical oceanography, 133(623), 347-362.

Roberts, N.M. (2003) The impact of a change to the use of the convection scheme to high-resolution simulations of convective events. Met Office Forecasting Research Technical Report number: 407.

Roberts, N. M., & Lean, H. W. (2008). Scale-selective verification of rainfall accumulations from high-resolution forecasts of convective events. Monthly Weather Review, 136(1), 78-97.

Romero, R., Guijarro, J. A., Ramis, C., & Alonso, S. (1998). A 30-year (1964–1993) daily rainfall data base for the Spanish Mediterranean regions: First exploratory study. International Journal of Climatology: A Journal of the Royal Meteorological Society, 18(5), 541-560.

Romine, G. S., Schwartz, C. S., Snyder, C., Anderson, J. L., & Weisman, M. L. (2013). Model bias in a continuously cycled assimilation system and its influence on convection-permitting forecasts. Monthly weather review, 141(4), 1263-1284.

Schwartz, C. S., Kain, J. S., Weiss, S. J., Xue, M., Bright, D. R., Kong, F., ... & Wandishin, M. S. (2010). Toward improved convection-allowing ensembles: Model physics sensitivities and optimizing probabilistic guidance with small ensemble membership. Weather and Forecasting, 25(1), 263-280.

Scott, D. W. (2015). Multivariate density estimation: theory, practice, and visualization. John Wiley & Sons.

Shen, F., Song, L., Li, H., He, Z., & Xu, D. (2022). Effects of different momentum control variables in radar data assimilation on the analysis and forecast of strong convective systems under the background of northeast cold vortex. Atmospheric Research, 280, 106415.

Silverman, B. W. (2018). Density estimation for statistics and data analysis. Routledge.

Skamarock, W. C., Klemp, J. B., Dudhia, J., Gill, D. O., Barker, D. M., Wang, W., & Powers, J. G. (2008). A description of the advanced research WRF version 3. National Center For Atmospheric Research Boulder Co Mesoscale and Microscale Meteorology Div.

Stanski, H.R., L.J. Wilson, and W.R. Burrows, 1989: Survey of common verification methods in meteorology. World Weather Watch Tech. Rept. No.8, WMO/TD No.358, WMO, Geneva, 114 pp.

Stensrud, D. J., Bao, J. W., & Warner, T. T. (2000). Using initial condition and model physics perturbations in short-range ensemble simulations of mesoscale convective systems. Monthly Weather Review, 128(7), 2077-2107.

Stensrud, D. J., Xue, M., Wicker, L. J., Kelleher, K. E., Foster, M. P., Schaefer, J. T., ... & Tuell, J. P. (2009). Convective-scale warn-on-forecast system: A vision for 2020. Bulletin of the American Meteorological Society, 90(10), 1487-1500.

Sun, J., & Crook, N. A. (1997). Dynamical and microphysical retrieval from Doppler radar observations using a cloud model and its adjoint. Part I: Model development and simulated data experiments. Journal of the Atmospheric Sciences, 54(12), 1642-1661.

Swets, J. A. (1973). The Relative Operating Characteristic in Psychology: A technique for isolating effects of response bias finds wide use in the study of perception and cognition. Science, 182(4116), 990-1000.

Tewari, M., Chen, M., Wang, F., Dudhia, W., LeMone, J., Mitchell, K., Ek, M., Gayno, G., Wegiel, J., and Cuenca, R. H. (2004, January). Implementation and verification of the unified NOAH land surface model in the WRF model (Formerly Paper Number 17.5). In Proceedings of the 20th conference on weather analysis and forecasting/16th conference on numerical weather prediction, Seattle, WA, USA (Vol. 14).

Taylor, K. E. (2001). Summarizing multiple aspects of model performance in a single diagram. Journal of geophysical research: atmospheres, 106(D7), 7183-7192.

Tiedtke, M. I. C. H. A. E. L. (1989). A comprehensive mass flux scheme for cumulus parameterization in large-scale models. Monthly weather review, 117(8), 1779-1800.

Thompson, G., Field, P. R., Rasmussen, R. M., & Hall, W. D. (2008). Explicit forecasts of winter precipitation using an improved bulk microphysics scheme. Part II: Implementation of a new snow parameterization. Monthly Weather Review, 136(12), 5095-5115.

Tong, M., & Xue, M. (2005). Ensemble Kalman filter assimilation of Doppler radar data with a compressible nonhydrostatic model: OSS experiments. Monthly Weather Review, 133(7), 1789-1807.

Torcasio, R. C., Federico, S., Comellas Prat, A., Panegrossi, G., D'Adderio, L. P., & Dietrich, S. (2021). Impact of lightning data assimilation on the short-term precipitation forecast over the Central Mediterranean Sea. Remote Sensing, 13(4), 682.

Tukey, J. W. (1977). Exploratory data analysis (Vol. 2, pp. 131-160).

Van Leeuwen, P. J. (2009). Particle filtering in geophysical systems. Monthly Weather Review, 137(12), 4089-4114.

Velden, C., Lewis, W. E., Bresky, W., Stettner, D., Daniels, J., & Wanzong, S. (2017). Assimilation of high-resolution satellite-derived atmospheric motion vectors: Impact on HWRF forecasts of tropical cyclone track and intensity. Monthly Weather Review, 145(3), 1107-1125.

Wang, H., Huang, X. Y., Sun, J., Xu, D., Fan, S., Zhong, J., & Zhang, M. (2013, September). A comparison between the 3/4DVAR and hybrid ensemble-VAR techniques for radar data assimilation. In 35th Conference on Radar Meteorology, Breckenridge.

Wang, Y., Yussouf, N., Kerr, C. A., Stratman, D. R., & Matilla, B. C. (2022). An experimental 1-km Warn-on-Forecast System for hazardous weather events. Monthly Weather Review, 150(11), 3081-3102.

Wheatley, D. M., Stensrud, D. J., Dowell, D. C., & Yussouf, N. (2012). Application of a WRF mesoscale data assimilation system to springtime severe weather events 2007–09. Monthly weather review, 140(5), 1539-1557.

Whitaker, J. S., Hamill, T. M., Wei, X., Song, Y., & Toth, Z. (2008). Ensemble data assimilation with the NCEP global forecast system. *Monthly Weather Review*, *136*(2), 463-482.

Con formato: Fuente: Cursiva, Color de fuente: Azul, Resaltar

Con formato: Interlineado: sencillo

Wu, X., Zhang, S., Liu, Z., Rosati, A., & Delworth, T. L. (2013). A study of impact of the geographic dependence of observing system on parameter estimation with an intermediate coupled model. Climate Dynamics, 40, 1789-1798.

Xiao, Q., & Sun, J. (2007). Multiple-radar data assimilation and short-range quantitative precipitation forecasting of a squall line observed during IHOP_2002. Monthly Weather Review, 135(10), 3381-3404.

Yano, J. I., Ziemiański, M. Z., Cullen, M., Termonia, P., Onvlee, J., Bengtsson, L., ... & Wyszogrodzki, A. A. (2018). Scientific challenges of convective-scale numerical weather prediction. Bulletin of the American Meteorological Society, 99(4), 699-710.

Yussouf, N., Dowell, D. C., Wicker, L. J., Knopfmeier, K. H., & Wheatley, D. M. (2015). Storm-scale data assimilation and ensemble forecasts for the 27 April 2011 severe weather outbreak in Alabama. Monthly Weather Review, 143(8), 3044-3066.

Eliminado: ¶

Appendix

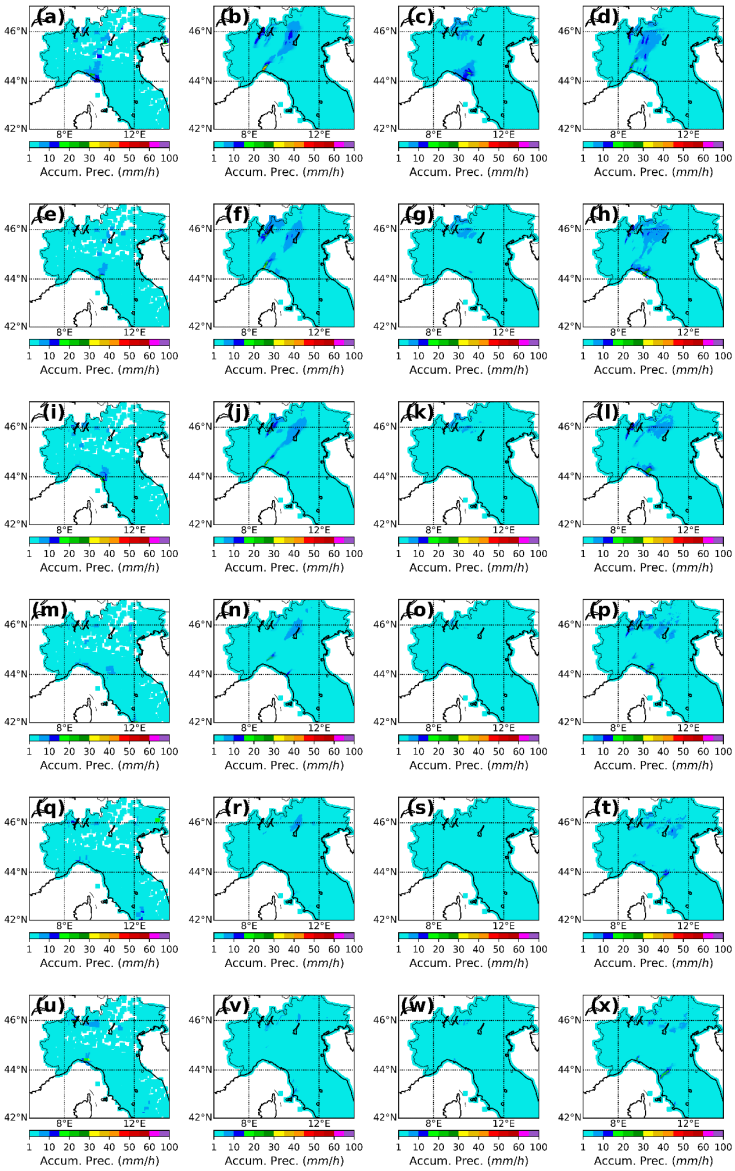

2625
2626
2627

Fig. A1. 1-h accumulated precipitation computed from 00-06 UTC 15 October 2012 associated with Observations (first column), NODA (second column), EnKF (CNTRL) (third column) and 3DVar (CNTRL) (fourth column).

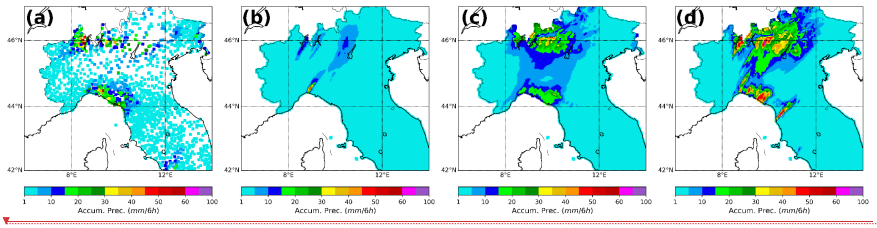

Fig. A2. 6-h accumulated precipitation computed from 00-06 UTC 15 October 2012 associated with (a) Observations, (b) NODA, (c) EnKF (CNTRL), (d) 3DVar (CNTRL).

Author Contribution

D. S. Carrió: Conceptualization, Methodology, Software, Validation, Formal analysis, investigation, writing-original draft, writing-review & editing, visualization, supervision; **V. Mazzarella:** formal analysis, writing-review; **R. Ferretti**: formal analysis, writing-review, supervision.

Competing Interests

The authors declare that they have no conflict of interest.

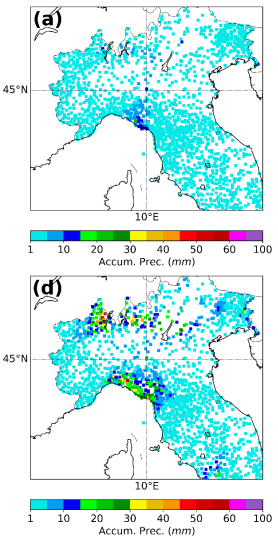

Eliminado:
Eliminado: l
Eliminado: (a)
Eliminado: (b)
Eliminado: (c)
Eliminado: ¶
Eliminado: ¶
Eliminado: d
Eliminado: e
Eliminado:
Eliminado: f
Eliminado: ¶

Página 5: [1] Eliminado	**Diego Saúl Carrió Carrió**	**19/2/25 8:48:00**
Página 5: [2] Eliminado	**Diego Saúl Carrió Carrió**	**19/2/25 8:48:00**
Página 5: [3] Eliminado	**Diego Saúl Carrió Carrió**	**19/2/25 8:48:00**
Página 5: [4] Eliminado	**Diego Saúl Carrió Carrió**	**19/2/25 8:48:00**
Página 5: [5] Eliminado	**Diego Saúl Carrió Carrió**	**19/2/25 8:48:00**
Página 5: [6] Eliminado	**Diego Saúl Carrió Carrió**	**19/2/25 8:48:00**
Página 5: [7] Eliminado	**Diego Saúl Carrió Carrió**	**19/2/25 8:48:00**
Página 5: [8] Eliminado	**Diego Saúl Carrió Carrió**	**19/2/25 8:56:00**
Página 5: [8] Eliminado	**Diego Saúl Carrió Carrió**	**19/2/25 8:56:00**
Página 5: [9] Eliminado	**Diego Saúl Carrió Carrió**	**19/2/25 8:56:00**
Página 5: [10] Eliminado	**Diego Saúl Carrió Carrió**	**19/2/25 8:56:00**
Página 5: [11] Eliminado	**Diego Saúl Carrió Carrió**	**19/2/25 8:56:00**
Página 5: [11] Eliminado	**Diego Saúl Carrió Carrió**	**19/2/25 8:56:00**
Página 5: [12] Eliminado	**Diego Saúl Carrió Carrió**	**19/2/25 8:56:00**
Página 5: [13] Eliminado	**Diego Saúl Carrió Carrió**	**19/2/25 8:56:00**

Página 5: [13] Eliminado	**Diego Saúl Carrió Carrió**	**19/2/25 8:56:00**

Página 5: [14] Eliminado	**Diego Saúl Carrió Carrió**	**19/2/25 8:56:00**

Página 5: [14] Eliminado	**Diego Saúl Carrió Carrió**	**19/2/25 8:56:00**

Página 5: [15] Eliminado	**Diego Saúl Carrió Carrió**	**19/2/25 8:56:00**

Página 5: [15] Eliminado	**Diego Saúl Carrió Carrió**	**19/2/25 8:56:00**

Página 5: [16] Eliminado	**Diego Saúl Carrió Carrió**	**19/2/25 8:56:00**

Página 23: [17] Eliminado	**Diego Saúl Carrió Carrió**	**5/3/25 11:31:00**

Página 23: [18] Eliminado	**Diego Saúl Carrió Carrió**	**5/3/25 11:31:00**

Página 23: [19] Eliminado	**Diego Saúl Carrió Carrió**	**5/3/25 11:31:00**

Página 23: [20] Eliminado	**Diego Saúl Carrió Carrió**	**5/3/25 11:31:00**

Página 24: [21] Eliminado	**Diego Saúl Carrió Carrió**	**6/3/25 10:35:00**

Página 26: [22] Eliminado	**Diego Saúl Carrió Carrió**	**6/3/25 10:53:00**

Página 26: [23] Con formato	**Diego Saúl Carrió Carrió**	**4/3/25 12:32:00**

Fuente: 12 pto, Negrita

Página 26: [23] Con formato	**Diego Saúl Carrió Carrió**	**4/3/25 12:32:00**

Fuente: 12 pto, Negrita

Página 29: [24] Eliminado	**Diego Saúl Carrió Carrió**	**6/3/25 11:45:00**

Página 29: [25] Eliminado **Diego Saúl Carrió Carrió** **6/3/25 11:45:00**

Página 29: [26] Eliminado **Diego Saúl Carrió Carrió** **6/3/25 11:45:00**

Página 29: [27] Eliminado **Diego Saúl Carrió Carrió** **6/3/25 11:45:00**

Página 29: [28] Eliminado **Diego Saúl Carrió Carrió** **6/3/25 11:45:00**

Página 31: [29] Con formato **Diego Saúl Carrió Carrió** **4/3/25 13:25:00**

Fuente: 13 pto, Negrita, Color de fuente: Azul

Página 31: [30] Con formato **Diego Saúl Carrió Carrió** **4/3/25 13:25:00**

Fuente: 13 pto, Negrita, Color de fuente: Azul

Página 31: [31] Con formato **Diego Saúl Carrió Carrió** **4/3/25 13:25:00**

Fuente: 13 pto, Negrita, Color de fuente: Azul

Página 31: [32] Con formato **Diego Saúl Carrió Carrió** **4/3/25 13:26:00**

Justificado, Espacio Antes: 0 pto

Página 31: [33] Con formato **Diego Saúl Carrió Carrió** **4/3/25 13:26:00**

Fuente: 13 pto, Negrita, Color de fuente: Azul

Página 31: [34] Con formato **Diego Saúl Carrió Carrió** **4/3/25 13:26:00**

Fuente: 13 pto, Negrita, Color de fuente: Azul

Página 31: [35] Con formato **Diego Saúl Carrió Carrió** **4/3/25 13:26:00**

Fuente: 13 pto, Negrita, Color de fuente: Azul

Página 31: [36] Con formato **Diego Saúl Carrió Carrió** **4/3/25 13:26:00**

Fuente: 13 pto, Negrita, Color de fuente: Azul

Página 31: [37] Con formato **Diego Saúl Carrió Carrió** **4/3/25 13:26:00**

Fuente: 13 pto, Negrita, Color de fuente: Azul

Página 31: [38] Con formato **Diego Saúl Carrió Carrió** **4/3/25 13:26:00**

Fuente: 13 pto, Negrita, Color de fuente: Azul

Página 31: [39] Con formato **Diego Saúl Carrió Carrió** **4/3/25 13:26:00**

Fuente: 13 pto, Negrita, Color de fuente: Azul

Página 31: [40] Con formato **Diego Saúl Carrió Carrió** **4/3/25 13:26:00**

Fuente: 13 pto, Negrita, Color de fuente: Azul

Página 31: [41] Con formato **Diego Saúl Carrió Carrió** **4/3/25 13:26:00**

Fuente: 13 pto, Negrita, Color de fuente: Azul

Página 31: [42] Con formato **Diego Saúl Carrió Carrió** **4/3/25 13:26:00**

Fuente: 13 pto, Negrita, Color de fuente: Azul

Página 31: [43] Con formato	**Diego Saúl Carrió Carrió**	**4/3/25 13:26:00**

Fuente: 13 pto, Negrita, Color de fuente: Azul

Página 31: [44] Con formato	**Diego Saúl Carrió Carrió**	**4/3/25 13:26:00**

Fuente: 13 pto, Negrita, Color de fuente: Azul

Página 31: [45] Con formato	**Diego Saúl Carrió Carrió**	**4/3/25 13:26:00**

Fuente: 13 pto, Negrita, Color de fuente: Azul

Página 31: [46] Con formato	**Diego Saúl Carrió Carrió**	**4/3/25 13:26:00**

Fuente: 13 pto, Negrita, Color de fuente: Azul

Página 31: [47] Con formato	**Diego Saúl Carrió Carrió**	**4/3/25 13:26:00**

Fuente: 13 pto, Color de fuente: Azul

Página 31: [48] Con formato	**Diego Saúl Carrió Carrió**	**4/3/25 13:26:00**

Fuente: 13 pto, Color de fuente: Azul

Página 31: [49] Con formato	**Diego Saúl Carrió Carrió**	**4/3/25 13:26:00**

Fuente: 13 pto, Negrita, Color de fuente: Azul

Página 31: [50] Con formato	**Diego Saúl Carrió Carrió**	**4/3/25 13:26:00**

Fuente: 13 pto, Negrita, Color de fuente: Azul

Página 31: [51] Con formato	**Diego Saúl Carrió Carrió**	**4/3/25 13:26:00**

Fuente: 13 pto, Negrita, Color de fuente: Azul

Página 31: [52] Con formato	**Diego Saúl Carrió Carrió**	**4/3/25 13:26:00**

Fuente: 13 pto, Negrita, Color de fuente: Azul

Página 31: [53] Con formato	**Diego Saúl Carrió Carrió**	**4/3/25 13:26:00**

Fuente: 13 pto, Negrita, Color de fuente: Azul

Página 31: [54] Con formato	**Diego Saúl Carrió Carrió**	**4/3/25 13:26:00**

Fuente: 13 pto, Negrita, Color de fuente: Azul

Página 31: [55] Con formato	**Diego Saúl Carrió Carrió**	**4/3/25 13:26:00**

Fuente: 13 pto, Negrita, Color de fuente: Azul

Página 31: [56] Con formato	**Diego Saúl Carrió Carrió**	**4/3/25 13:26:00**

Fuente: 13 pto, Negrita, Color de fuente: Azul

Página 31: [57] Con formato	**Diego Saúl Carrió Carrió**	**4/3/25 13:26:00**

Fuente: 13 pto, Negrita, Color de fuente: Azul

Página 31: [58] Con formato	**Diego Saúl Carrió Carrió**	**4/3/25 13:26:00**

Fuente: 13 pto, Negrita, Color de fuente: Azul

Página 31: [59] Con formato	**Diego Saúl Carrió Carrió**	**4/3/25 13:26:00**

Fuente: 13 pto, Negrita, Color de fuente: Azul

Página 31: [60] Con formato	**Diego Saúl Carrió Carrió**	**4/3/25 13:26:00**

Fuente: 13 pto, Negrita, Color de fuente: Azul

Página 31: [61] Con formato	**Diego Saúl Carrió Carrió**	**4/3/25 13:26:00**

Fuente: 13 pto, Negrita, Color de fuente: Azul

Página 31: [62] Con formato	**Diego Saúl Carrió Carrió**	**4/3/25 13:26:00**

Fuente: 13 pto, Negrita, Color de fuente: Azul

Página 31: [63] Con formato	**Diego Saúl Carrió Carrió**	**4/3/25 13:26:00**

Fuente: 13 pto, Negrita, Color de fuente: Azul

Página 31: [64] Eliminado	**Diego Saúl Carrió Carrió**	**19/2/25 9:44:00**

Página 31: [65] Con formato	**Diego Saúl Carrió Carrió**	**4/3/25 13:26:00**

Fuente: 13 pto, Negrita, Color de fuente: Azul

Página 31: [66] Eliminado	**Diego Saúl Carrió Carrió**	**19/2/25 9:38:00**

Página 31: [67] Con formato	**Diego Saúl Carrió Carrió**	**4/3/25 13:26:00**

Fuente: 13 pto, Negrita, Color de fuente: Azul

Página 31: [68] Con formato	**Diego Saúl Carrió Carrió**	**4/3/25 13:26:00**

Fuente: 13 pto, Negrita, Color de fuente: Azul

Página 31: [69] Con formato	**Diego Saúl Carrió Carrió**	**4/3/25 13:26:00**

Fuente: 13 pto, Negrita, Color de fuente: Azul

Página 31: [70] Con formato	**Diego Saúl Carrió Carrió**	**4/3/25 13:26:00**

Fuente: 13 pto, Negrita, Color de fuente: Azul

Página 31: [71] Con formato	**Diego Saúl Carrió Carrió**	**4/3/25 13:26:00**

Fuente: 13 pto, Negrita, Color de fuente: Azul

Página 31: [72] Con formato	**Diego Saúl Carrió Carrió**	**4/3/25 13:26:00**

Fuente: 13 pto, Negrita, Color de fuente: Azul

Página 31: [73] Con formato	**Diego Saúl Carrió Carrió**	**4/3/25 13:26:00**

Fuente: 13 pto, Negrita, Color de fuente: Azul

Página 31: [74] Con formato	**Diego Saúl Carrió Carrió**	**4/3/25 13:26:00**

Fuente: 13 pto, Negrita, Color de fuente: Azul

Página 31: [75] Con formato	**Diego Saúl Carrió Carrió**	**4/3/25 13:26:00**

Fuente: 13 pto, Negrita, Color de fuente: Azul

Página 31: [76] Con formato	**Diego Saúl Carrió Carrió**	**4/3/25 13:26:00**

Fuente: 13 pto, Negrita, Color de fuente: Azul

Página 31: [77] Con formato	**Diego Saúl Carrió Carrió**	**4/3/25 13:26:00**

Fuente: 13 pto, Negrita, Color de fuente: Azul

Página 31: [78] Con formato	**Diego Saúl Carrió Carrió**	**4/3/25 13:26:00**

Fuente: 13 pto, Negrita, Color de fuente: Azul

Página 31: [79] Con formato	**Diego Saúl Carrió Carrió**	**4/3/25 13:26:00**

Fuente: 13 pto, Negrita, Color de fuente: Azul

Página 31: [80] Con formato	**Diego Saúl Carrió Carrió**	**4/3/25 13:26:00**

Fuente: 13 pto, Negrita, Color de fuente: Azul

Página 32: [81] Con formato	**Diego Saúl Carrió Carrió**	**4/3/25 13:26:00**

Fuente: 13 pto, Negrita, Color de fuente: Azul

Página 32: [82] Con formato	**Diego Saúl Carrió Carrió**	**4/3/25 13:26:00**

Fuente: 13 pto, Negrita, Color de fuente: Azul

Página 32: [83] Con formato	**Diego Saúl Carrió Carrió**	**4/3/25 13:26:00**

Fuente: 13 pto, Negrita, Color de fuente: Azul

Página 32: [84] Con formato	**Diego Saúl Carrió Carrió**	**4/3/25 13:26:00**

Fuente: 13 pto, Negrita, Color de fuente: Azul

Página 32: [85] Con formato	**Diego Saúl Carrió Carrió**	**4/3/25 13:26:00**

Fuente: 13 pto, Negrita, Color de fuente: Azul

Página 32: [86] Con formato	**Diego Saúl Carrió Carrió**	**4/3/25 13:26:00**

Fuente: 13 pto, Negrita, Color de fuente: Azul

Página 32: [87] Con formato	**Diego Saúl Carrió Carrió**	**4/3/25 13:26:00**

Fuente: 13 pto, Negrita, Color de fuente: Azul

Página 32: [88] Con formato	**Diego Saúl Carrió Carrió**	**4/3/25 13:26:00**

Fuente: 13 pto, Negrita, Color de fuente: Azul

Página 32: [89] Con formato	**Diego Saúl Carrió Carrió**	**4/3/25 13:26:00**

Fuente: 13 pto, Negrita, Color de fuente: Azul

Página 32: [90] Con formato	**Diego Saúl Carrió Carrió**	**4/3/25 13:26:00**

Fuente: 13 pto, Negrita, Color de fuente: Azul

Página 32: [91] Eliminado	**Diego Saúl Carrió Carrió**	**19/2/25 9:50:00**

Página 32: [91] Eliminado	**Diego Saúl Carrió Carrió**	**19/2/25 9:50:00**

Página 32: [92] Con formato	**Diego Saúl Carrió Carrió**	**4/3/25 13:26:00**

Fuente: 13 pto, Negrita, Color de fuente: Azul

Página 32: [93] Eliminado	**Diego Saúl Carrió Carrió**	**19/2/25 9:54:00**

Página 32: [94] Con formato	**Diego Saúl Carrió Carrió**	**4/3/25 13:26:00**

Fuente: 13 pto, Negrita, Color de fuente: Azul

Página 32: [95] Con formato	**Diego Saúl Carrió Carrió**	**4/3/25 13:26:00**

Fuente: 13 pto, Negrita, Color de fuente: Azul

Página 32: [96] Con formato	Diego Saúl Carrió Carrió	4/3/25 13:26:00

Fuente: 13 pto, Negrita, Color de fuente: Azul

Página 32: [97] Con formato	Diego Saúl Carrió Carrió	4/3/25 13:26:00

Fuente: 13 pto, Negrita, Color de fuente: Azul

Página 32: [98] Con formato	Diego Saúl Carrió Carrió	4/3/25 13:26:00

Fuente: 13 pto, Negrita, Color de fuente: Azul

Página 32: [99] Con formato	Diego Saúl Carrió Carrió	4/3/25 13:26:00

Fuente: 13 pto, Negrita, Color de fuente: Azul

Página 32: [100] Con formato	Diego Saúl Carrió Carrió	4/3/25 13:26:00

Fuente: 13 pto, Negrita, Color de fuente: Azul

Página 32: [101] Con formato	Diego Saúl Carrió Carrió	4/3/25 13:26:00

Fuente: 13 pto, Negrita, Color de fuente: Azul

Página 32: [102] Con formato	Diego Saúl Carrió Carrió	4/3/25 13:26:00

Fuente: 13 pto, Negrita, Color de fuente: Azul

Página 32: [103] Con formato	Diego Saúl Carrió Carrió	4/3/25 13:26:00

Fuente: 13 pto, Negrita, Color de fuente: Azul

Página 32: [104] Con formato	Diego Saúl Carrió Carrió	4/3/25 13:26:00

Fuente: 13 pto, Negrita, Color de fuente: Azul

Página 32: [105] Con formato	Diego Saúl Carrió Carrió	4/3/25 13:26:00

Fuente: 13 pto, Negrita, Color de fuente: Azul

Página 32: [106] Con formato	Diego Saúl Carrió Carrió	4/3/25 13:26:00

Fuente: 13 pto, Negrita, Color de fuente: Azul

Página 32: [107] Con formato	Diego Saúl Carrió Carrió	4/3/25 13:26:00

Fuente: 13 pto, Negrita, Sin Cursiva, Color de fuente: Azul

Página 32: [108] Con formato	Diego Saúl Carrió Carrió	4/3/25 13:26:00

Fuente: 13 pto, Negrita, Color de fuente: Azul

Página 32: [109] Con formato	Diego Saúl Carrió Carrió	4/3/25 13:26:00

Fuente: 13 pto, Negrita, Sin Cursiva, Color de fuente: Azul

Página 32: [110] Con formato	Diego Saúl Carrió Carrió	4/3/25 13:26:00

Fuente: 13 pto, Negrita, Color de fuente: Azul

Página 32: [111] Con formato	Diego Saúl Carrió Carrió	4/3/25 13:26:00

Fuente: 13 pto, Negrita, Color de fuente: Azul

Página 32: [112] Con formato	Diego Saúl Carrió Carrió	4/3/25 13:26:00

Fuente: 13 pto, Negrita, Color de fuente: Azul

Página 32: [113] Con formato	Diego Saúl Carrió Carrió	4/3/25 13:26:00

Fuente: 13 pto, Negrita, Sin Cursiva, Color de fuente: Azul

Página 32: [114] Con formato	Diego Saúl Carrió Carrió	4/3/25 13:26:00

Fuente: 13 pto, Negrita, Color de fuente: Azul

Página 32: [115] Con formato	**Diego Saúl Carrió Carrió**	**4/3/25 13:26:00**

Fuente: 13 pto, Negrita, Sin Cursiva, Color de fuente: Azul

Página 32: [116] Con formato	**Diego Saúl Carrió Carrió**	**4/3/25 13:26:00**

Fuente: 13 pto, Negrita, Color de fuente: Azul

Página 32: [117] Con formato	**Diego Saúl Carrió Carrió**	**4/3/25 13:26:00**

Fuente: 13 pto, Negrita, Sin Cursiva, Color de fuente: Azul

Página 32: [118] Con formato	**Diego Saúl Carrió Carrió**	**4/3/25 13:26:00**

Fuente: 13 pto, Negrita, Color de fuente: Azul

Página 32: [119] Con formato	**Diego Saúl Carrió Carrió**	**4/3/25 13:26:00**

Fuente: 13 pto, Negrita, Sin Cursiva, Color de fuente: Azul

Página 32: [120] Con formato	**Diego Saúl Carrió Carrió**	**4/3/25 13:26:00**

Fuente: 13 pto, Negrita, Color de fuente: Azul

Página 32: [121] Con formato	**Diego Saúl Carrió Carrió**	**4/3/25 13:26:00**

Fuente: 13 pto, Negrita, Color de fuente: Azul

Página 32: [122] Con formato	**Diego Saúl Carrió Carrió**	**4/3/25 13:26:00**

Fuente: 13 pto, Negrita, Color de fuente: Azul

Página 32: [123] Con formato	**Diego Saúl Carrió Carrió**	**4/3/25 13:26:00**

Fuente: 13 pto, Negrita, Color de fuente: Azul

Página 32: [124] Con formato	**Diego Saúl Carrió Carrió**	**4/3/25 13:26:00**

Fuente: 13 pto, Negrita, Sin Cursiva, Color de fuente: Azul

Página 32: [125] Con formato	**Diego Saúl Carrió Carrió**	**4/3/25 13:26:00**

Fuente: 13 pto, Negrita, Color de fuente: Azul

Página 32: [126] Con formato	**Diego Saúl Carrió Carrió**	**4/3/25 13:26:00**

Fuente: 13 pto, Negrita, Color de fuente: Azul

Página 32: [127] Con formato	**Diego Saúl Carrió Carrió**	**4/3/25 13:26:00**

Fuente: 13 pto, Negrita, Sin Cursiva, Color de fuente: Azul

Página 32: [128] Con formato	**Diego Saúl Carrió Carrió**	**4/3/25 13:26:00**

Fuente: 13 pto, Negrita, Color de fuente: Azul

Página 32: [129] Con formato	**Diego Saúl Carrió Carrió**	**4/3/25 13:26:00**

Fuente: 13 pto, Negrita, Color de fuente: Azul

Página 32: [130] Con formato	**Diego Saúl Carrió Carrió**	**4/3/25 13:26:00**

Fuente: 13 pto, Negrita, Color de fuente: Azul

Página 32: [131] Con formato	**Diego Saúl Carrió Carrió**	**4/3/25 13:26:00**

Fuente: 13 pto, Negrita, Color de fuente: Azul

Página 32: [132] Con formato	**Diego Saúl Carrió Carrió**	**4/3/25 13:26:00**

Fuente: 13 pto, Negrita, Color de fuente: Azul

Página 32: [133] Con formato	**Diego Saúl Carrió Carrió**	**4/3/25 13:26:00**

Fuente: 13 pto, Negrita, Color de fuente: Azul

Página 32: [134] Con formato	**Diego Saúl Carrió Carrió**	**4/3/25 13:26:00**

Fuente: 13 pto, Negrita, Color de fuente: Azul

Página 32: [135] Con formato	**Diego Saúl Carrió Carrió**	**4/3/25 13:26:00**

Fuente: 13 pto, Negrita, Color de fuente: Azul

Página 32: [136] Con formato	**Diego Saúl Carrió Carrió**	**4/3/25 13:26:00**

Fuente: 13 pto, Negrita, Color de fuente: Azul

Página 32: [137] Con formato	**Diego Saúl Carrió Carrió**	**4/3/25 13:26:00**

Fuente: 13 pto, Negrita, Color de fuente: Azul

Página 32: [138] Con formato	**Diego Saúl Carrió Carrió**	**4/3/25 13:26:00**

Fuente: 13 pto, Negrita, Color de fuente: Azul

Página 32: [139] Eliminado	**Diego Saúl Carrió Carrió**	**5/3/25 11:13:00**

Página 32: [140] Con formato	**Diego Saúl Carrió Carrió**	**4/3/25 13:26:00**

Fuente: 13 pto, Negrita, Color de fuente: Azul

Página 32: [141] Con formato	**Diego Saúl Carrió Carrió**	**4/3/25 13:26:00**

Fuente: 13 pto, Negrita, Color de fuente: Azul

Página 32: [142] Con formato	**Diego Saúl Carrió Carrió**	**4/3/25 13:26:00**

Fuente: 13 pto, Negrita, Color de fuente: Azul

Página 32: [143] Con formato	**Diego Saúl Carrió Carrió**	**4/3/25 13:26:00**

Fuente: 13 pto, Negrita, Color de fuente: Azul

Página 32: [144] Con formato	**Diego Saúl Carrió Carrió**	**4/3/25 13:26:00**

Fuente: 13 pto, Negrita, Color de fuente: Azul

Página 32: [145] Con formato	**Diego Saúl Carrió Carrió**	**4/3/25 13:26:00**

Fuente: 13 pto, Negrita, Color de fuente: Azul

Página 32: [146] Con formato	**Diego Saúl Carrió Carrió**	**4/3/25 13:26:00**

Fuente: 13 pto, Negrita, Color de fuente: Azul

Página 32: [147] Con formato	**Diego Saúl Carrió Carrió**	**4/3/25 13:26:00**

Fuente: 13 pto, Negrita, Color de fuente: Azul

Página 32: [148] Con formato	**Diego Saúl Carrió Carrió**	**4/3/25 13:26:00**

Fuente: 13 pto, Negrita, Color de fuente: Azul

Página 32: [149] Con formato	**Diego Saúl Carrió Carrió**	**4/3/25 13:26:00**

Fuente: 13 pto, Negrita, Color de fuente: Azul, Sin Superíndice / Subíndice

Página 32: [150] Con formato	**Diego Saúl Carrió Carrió**	**4/3/25 13:26:00**

Fuente: 13 pto, Negrita, Color de fuente: Azul

Página 32: [151] Con formato	**Diego Saúl Carrió Carrió**	**4/3/25 13:26:00**

Fuente: 13 pto, Negrita, Color de fuente: Azul, Sin Superíndice / Subíndice

Página 32: [152] Con formato **Diego Saúl Carrió Carrió** **4/3/25 13:26:00**

Fuente: 13 pto, Negrita, Color de fuente: Azul

Página 33: [153] Eliminado **Diego Saúl Carrió Carrió** **15/3/25 10:52:00**

Página 34: [154] Con formato **Diego Saúl Carrió Carrió** **4/3/25 13:26:00**

Fuente: 13 pto, Color de fuente: Azul

Página 34: [155] Eliminado **Diego Saúl Carrió Carrió** **6/3/25 12:06:00**

Página 34: [156] Con formato **Diego Saúl Carrió Carrió** **4/3/25 13:26:00**

Fuente: Negrita, Color de fuente: Azul

Página 34: [157] Con formato **Diego Saúl Carrió Carrió** **4/3/25 13:26:00**

Fuente: (Predeterminada) Times New Roman, 13 pto, Negrita, Color de fuente: Azul

Página 34: [158] Con formato **Diego Saúl Carrió Carrió** **4/3/25 13:26:00**

Fuente: (Predeterminada) Times New Roman, 13 pto, Negrita, Color de fuente: Azul

Página 34: [159] Con formato **Diego Saúl Carrió Carrió** **4/3/25 13:26:00**

Fuente: (Predeterminada) Times New Roman, 13 pto, Negrita, Color de fuente: Azul

Página 34: [160] Con formato **Diego Saúl Carrió Carrió** **4/3/25 13:26:00**

Fuente: (Predeterminada) Times New Roman, 13 pto, Negrita, Color de fuente: Azul

Página 34: [161] Con formato **Diego Saúl Carrió Carrió** **4/3/25 13:26:00**

Fuente: (Predeterminada) Times New Roman, 13 pto, Negrita, Color de fuente: Azul

Página 34: [162] Con formato **Diego Saúl Carrió Carrió** **4/3/25 13:26:00**

Fuente: 13 pto, Color de fuente: Azul

Página 34: [163] Con formato **Diego Saúl Carrió Carrió** **4/3/25 13:26:00**

Fuente: 13 pto, Color de fuente: Azul

Página 34: [164] Con formato **Diego Saúl Carrió Carrió** **4/3/25 13:26:00**

Fuente: 13 pto, Color de fuente: Azul

Página 34: [165] Con formato **Diego Saúl Carrió Carrió** **4/3/25 13:26:00**

Fuente: 13 pto, Negrita, Color de fuente: Azul, Sin Resaltar

Página 34: [166] Con formato **Diego Saúl Carrió Carrió** **4/3/25 13:26:00**

Fuente: 13 pto, Negrita, Sin Cursiva, Color de fuente: Azul, Sin Resaltar

Página 34: [167] Con formato **Diego Saúl Carrió Carrió** **4/3/25 13:26:00**

Fuente: 13 pto, Negrita, Color de fuente: Azul, Sin Resaltar

Página 34: [168] Con formato **Diego Saúl Carrió Carrió** **4/3/25 13:26:00**

Fuente: 13 pto, Negrita, Sin Cursiva, Color de fuente: Azul, Sin Resaltar

Página 34: [169] Con formato **Diego Saúl Carrió Carrió** **4/3/25 13:26:00**

Fuente: 13 pto, Negrita, Color de fuente: Azul, Sin Resaltar

Página 34: [170] Con formato **Diego Saúl Carrió Carrió** **4/3/25 13:26:00**

Fuente: 13 pto, Negrita, Color de fuente: Azul, Sin Resaltar

Página 34: [171] Con formato **Diego Saúl Carrió Carrió** **4/3/25 13:26:00**

Fuente: 13 pto, Negrita, Color de fuente: Azul

Página 34: [172] Con formato **Diego Saúl Carrió Carrió** **4/3/25 13:26:00**

Fuente: 13 pto, Negrita, Color de fuente: Azul, Sin Resaltar

Página 34: [173] Con formato **Diego Saúl Carrió Carrió** **4/3/25 13:26:00**

Fuente: 13 pto, Negrita, Sin Cursiva, Color de fuente: Azul, Sin Resaltar

Página 34: [174] Con formato **Diego Saúl Carrió Carrió** **4/3/25 13:26:00**

Fuente: 13 pto, Negrita, Color de fuente: Azul, Sin Resaltar

Página 34: [175] Con formato **Diego Saúl Carrió Carrió** **4/3/25 13:26:00**

Fuente: 13 pto, Negrita, Sin Cursiva, Color de fuente: Azul, Sin Resaltar

Página 34: [176] Con formato **Diego Saúl Carrió Carrió** **4/3/25 13:26:00**

Fuente: 13 pto, Negrita, Color de fuente: Azul, Sin Resaltar

Página 34: [177] Con formato **Diego Saúl Carrió Carrió** **4/3/25 13:26:00**

Fuente: 13 pto, Negrita, Color de fuente: Azul, Sin Resaltar

Página 34: [178] Con formato **Diego Saúl Carrió Carrió** **4/3/25 13:26:00**

Fuente: 13 pto, Negrita, Color de fuente: Azul, Sin Resaltar

Página 34: [179] Con formato **Diego Saúl Carrió Carrió** **4/3/25 13:26:00**

Fuente: 13 pto, Negrita, Color de fuente: Azul, Sin Resaltar

Página 34: [180] Con formato **Diego Saúl Carrió Carrió** **4/3/25 13:26:00**

Fuente: 13 pto, Negrita, Sin Cursiva, Color de fuente: Azul, Sin Resaltar

Página 34: [181] Con formato **Diego Saúl Carrió Carrió** **4/3/25 13:26:00**

Fuente: 13 pto, Negrita, Color de fuente: Azul, Sin Resaltar

Página 34: [182] Con formato **Diego Saúl Carrió Carrió** **4/3/25 13:26:00**

Fuente: 13 pto, Negrita, Sin Cursiva, Color de fuente: Azul, Sin Resaltar

Página 34: [183] Con formato **Diego Saúl Carrió Carrió** **4/3/25 13:26:00**

Fuente: 13 pto, Negrita, Color de fuente: Azul, Sin Resaltar

Página 34: [184] Con formato **Diego Saúl Carrió Carrió** **4/3/25 13:26:00**

Fuente: 13 pto, Negrita, Color de fuente: Azul, Sin Resaltar

Página 34: [185] Con formato **Diego Saúl Carrió Carrió** **4/3/25 13:26:00**

Fuente: 13 pto, Negrita, Color de fuente: Azul

Página 34: [186] Con formato **Diego Saúl Carrió Carrió** **4/3/25 13:26:00**

Fuente: 13 pto, Negrita, Color de fuente: Azul

Página 34: [187] Con formato **Diego Saúl Carrió Carrió** **4/3/25 13:26:00**

Fuente: 13 pto, Negrita, Color de fuente: Azul

Página 34: [188] Con formato **Diego Saúl Carrió Carrió** **4/3/25 13:26:00**

Fuente: 13 pto, Negrita, Color de fuente: Azul

Página 34: [189] Con formato	**Diego Saúl Carrió Carrió**	**4/3/25 13:26:00**

Fuente: 13 pto, Negrita, Color de fuente: Azul

Página 34: [190] Con formato	**Diego Saúl Carrió Carrió**	**4/3/25 13:26:00**

Fuente: 13 pto, Negrita, Color de fuente: Azul

Página 34: [191] Con formato	**Diego Saúl Carrió Carrió**	**4/3/25 13:26:00**

Fuente: 13 pto, Negrita, Color de fuente: Azul

Página 34: [192] Con formato	**Diego Saúl Carrió Carrió**	**4/3/25 13:26:00**

Fuente: 13 pto, Negrita, Color de fuente: Azul

Página 34: [193] Con formato	**Diego Saúl Carrió Carrió**	**4/3/25 13:26:00**

Fuente: 13 pto, Negrita, Color de fuente: Azul

Página 34: [194] Con formato	**Diego Saúl Carrió Carrió**	**4/3/25 13:26:00**

Fuente: 13 pto, Negrita, Color de fuente: Azul

Página 34: [195] Con formato	**Diego Saúl Carrió Carrió**	**4/3/25 13:26:00**

Fuente: 13 pto, Negrita, Color de fuente: Azul

Página 34: [196] Con formato	**Diego Saúl Carrió Carrió**	**4/3/25 13:26:00**

Fuente: 13 pto, Negrita, Color de fuente: Azul

Página 34: [197] Con formato	**Diego Saúl Carrió Carrió**	**4/3/25 13:26:00**

Fuente: 13 pto, Negrita, Color de fuente: Azul

Página 34: [198] Con formato	**Diego Saúl Carrió Carrió**	**4/3/25 13:26:00**

Fuente: 13 pto, Negrita, Color de fuente: Azul

Página 34: [199] Con formato	**Diego Saúl Carrió Carrió**	**4/3/25 13:26:00**

Fuente: 13 pto, Negrita, Color de fuente: Azul